Advanced Control of the Dynamics of Basic Movements in a Hand Exoskeleton

Robert Alexis Gómez Giraldo, Oscar Andrés Meza Ortiz y Johan Sebastián Quitian Valderrama

Thesis for the Degree of Electronic Engineer

Supervisor
Rodolfo Villamizar Mejía
Doctor of Engineering

Co-Supervisor
María Solange Patiño Segura
Master of Science in Physiotherapy

Industrial University of Santander
Faculty of Engineering
School of Electrical, Electronic and Telecommunications Engineering
Electronic Engineering
Bucaramanga
2026

Dedication

Robert Gomez: To my aunts, Alix Gómez and Yira Gómez, who became my family and unwavering support throughout these years. Your love, sacrifices, and constant encouragement made this achievement possible. To my mother, whose teachings, values, and guidance have shaped the person I am today. To my sister, for being a strong and exemplary woman whose resilience and determination have always inspired me. This achievement is dedicated to all of you, with my deepest gratitude and affection.

Oscar Meza: I dedicate this achievement, first and foremost, to God, for guiding me throughout this journey and allowing me to complete one of the most important stages of my life. To my parents, because this project is the result of the values instilled in me from an early age. From my father Oscar Meza, I inherited the value of hard work and the determination to move forward even in the most difficult moments; from my mother, Mariluz Ortiz, I inherited discipline and the conviction that great goals are achieved through perseverance. I owe much of the person I am today to them. Thank you for your unconditional support, for believing in my abilities, and for always encouraging me to give my very best. To my sister, Mariana Meza, for being my greatest motivation. Her presence has inspired me to be a role model, to take on responsibilities with greater maturity, and to strive every day to build a better future for my loved ones. To my grandmother, Paulina Cediel, for her dedication during my early years and for the values she instilled in me from childhood. Her love and care have been a fundamental part of my upbringing. Without all of you, achieving this dream would not have been as meaningful or rewarding. You have been part of my story and helped build the foundation for many of the achievements yet to come.

Acknowledgements

Robert Gomez: I would like to express my sincere gratitude to my friends for their unconditional support, companionship, and encouragement throughout my undergraduate studies. Their presence made this journey both more enjoyable and more meaningful. I am especially grateful to my teammates, Oscar Andrés Meza Ortiz and Johan Sebastián Quitian Valderrama, for their dedication, teamwork, and commitment throughout the development of this project. Working alongside them was both a privilege and a valuable learning experience. I would also like to thank the CEMOS research group for providing an environment that fostered learning, research, and professional growth. Finally, I extend my deepest appreciation to Professor Rodolfo Villamizar for giving us the opportunity to develop a project of such high academic and technical excellence. To everyone who contributed, directly or indirectly, to this achievement, thank you.

Oscar Meza: I would like to express my sincere gratitude to my thesis teammates for their commitment, dedication, and shared effort throughout the development of this project. Every challenge we overcame was made possible through teamwork and the knowledge we exchanged along the way. I am also grateful to my friends for their friendship and companionship throughout this stage of my life. Thank you for the shared experiences, conversations, and moments that made this journey more meaningful. I would like to extend special thanks to Robert Gómez, Santiago Castro, and Carlos Cala, whose friendship and support were present during important moments of this process. I would also like to thank the CEMOS Research Group and our advisor, Rodolfo Villamizar, for giving me the opportunity to develop this project and for contributing to my academic and professional growth throughout this process. Finally, I would like to thank everyone who, directly or indirectly, contributed to the development of this project and to my personal and professional growth.

Contents

List of Tables

List of Figures

List of Appendices

The appendices supporting this thesis are available for consultation through the UIS Library Database. The appendices included in this work are listed below:

Appendix A – ESP32 Identification

Appendix B – TXT Data Files

Appendix C – Simulation Figures and Results

Appendix D – ESP32 ADRC Implementation

Appendix E – PCB Design

Appendix F – Simulations

Appendix G – QFT Controller Design

Appendix H – ESP32 QFT Implementation

Resumen

Título: Control Avanzado de la Dinámica de Movimientos Básicos de un Exoesqueleto de Mano

Autores: R. Gomez, O. Meza, J. Quitian

Palabras Clave: Exoesqueleto de mano, Rehabilitación robótica, ADRC, QFT, Control robusto, Identificación de sistemas

Descripción:

Los sistemas de control para exoesqueletos de mano destinados a la rehabilitación post-accidente cerebrovascular enfrentan desafíos asociados a la variabilidad del paciente, las perturbaciones mecánicas y las incertidumbres del modelo, lo que puede reducir la efectividad de los enfoques de control convencionales. Estas dificultades se deben a la naturaleza no lineal, acoplada y altamente cambiante del sistema, donde las condiciones de operación pueden variar de forma significativa entre usuarios y sesiones de uso. Para abordar estas limitaciones, en este trabajo se implementan y comparan dos estrategias de control avanzado: el Control por Rechazo Activo de Perturbaciones (ADRC) y el Control Robusto basado en la Teoría de la Realimentación Cuantitativa (QFT). Se obtiene un modelo dinámico del sistema mediante modelado físico e identificación experimental de un exoesqueleto de mano desarrollado para pruebas de laboratorio, considerando tanto su dinámica mecánica como las perturbaciones externas presentes durante la operación. A partir de este modelo, ambos controladores son diseñados y evaluados mediante métricas de desempeño como el error de seguimiento y el esfuerzo de control. Los resultados muestran un compromiso entre precisión y esfuerzo de control. El controlador QFT requiere mayor acción de control y presenta variaciones de desempeño según las condiciones de operación, mientras que el controlador ADRC muestra un comportamiento más consistente, con menores errores de seguimiento y mayor robustez frente a perturbaciones, ruido y cambios de carga. Estos resultados contribuyen al desarrollo de estrategias de control más robustas, eficientes y adaptativas para sistemas de rehabilitación robótica.

Trabajo de Grado

Facultad de Ingenierías Fisicomecánicas – Escuela de Ingenierías Eléctrica, Electrónica y de Telecomunicaciones.

Abstract

Title: Advanced Control of the Dynamics of Basic Movements in a Hand Exoskeleton

Authors: R. Gomez, O. Meza, J. Quitian

Key Words: Hand Exoskeleton, Robotic Rehabilitation, ADRC, QFT, Robust Control, System Identification

Control systems for hand exoskeletons intended for post-stroke rehabilitation face challenges related to patient variability, mechanical disturbances, and model uncertainties, which can reduce the effectiveness of conventional control approaches. These difficulties arise from the nonlinear, coupled, and highly time-varying nature of the system, where operating conditions may change significantly between users and usage sessions. To address these limitations, this work implements and compares two advanced control strategies: Active Disturbance Rejection Control (ADRC) and Robust Control based on Quantitative Feedback Theory (QFT). A dynamic model of the system is obtained through physical modeling and experimental identification of a laboratory hand exoskeleton, considering both its mechanical dynamics and the external disturbances present during operation. Based on this model, both controllers are designed and evaluated using performance metrics such as tracking error and control effort. The results show a trade-off between accuracy and control effort. The QFT controller requires higher control action and exhibits performance variations under different operating conditions, while the ADRC controller shows more consistent behavior, with lower tracking errors and greater robustness against disturbances, noise, and load variations. These results contribute to the development of more robust, efficient, and adaptive control strategies for robotic rehabilitation systems.

Undergraduate Thesis

Faculty of Engineering – School of Electrical, Electronic and Telecommunications Engineering.

Introduction

A stroke is a medical emergency caused by an interruption of blood flow to the brain, either due to vascular occlusion (ischemia) or the rupture of a blood vessel (hemorrhage). Stroke is one of the leading causes of disability and mortality worldwide. Approximately 15 million people are affected by this condition each year, of whom around 5 million die and another 5 million suffer permanent impairments that affect the motor function of one or more limbs (Rosewilliam et al., 2014).

Among the most common motor impairments following stroke are those affecting the upper limb, particularly hand function. In severe cases, spasticity and involuntary co-contraction of antagonist muscles hinder the execution of functional hand movements (Barry et al., 2022). However, technological advancements have enabled the development of new therapeutic tools aimed at enhancing recovery processes. Among these, robotic rehabilitation systems, particularly exoskeletons, have emerged as a promising alternative to assist and guide hand movements during therapy (Mathonsi et al., 2024a).

These systems may be constructed using rigid structures or soft materials and typically integrate sensors, actuators, and control systems to generate precise and coordinated movements. In the context of motor rehabilitation, such devices have demonstrated therapeutic benefits by facilitating assisted finger flexion and extension, promoting repetitive task execution to stimulate neuroplasticity, and contributing to the recovery of hand motor function (Gu et al., 2024a, 2024b; Mathonsi et al., 2024b).

Despite these advantages, the control problem in hand exoskeletons remains an open challenge. Classical control strategies have shown limitations in dynamic reference tracking, difficulties in parameter tuning, risks of over-assistance, and limited robustness to patient variability and mechanical disturbances (Jones et al., 2010; Worsnopp et al., 2007). In this context, it becomes necessary to explore control approaches that enhance both robustness and adaptability. To this end, this work proposes the application of advanced control techniques to regulate the motion dynamics of a hand exoskeleton.

The proposed solution consists of the implementation and evaluation of two control strategies: Active Disturbance Rejection Control (ADRC) and robust control based on Quantitative Feedback Theory (QFT), selected for their ability to handle external disturbances and ensure adequate performance under variations in system dynamics. On one hand, the ADRC approach treats unmodeled dynamics and variations in patient condition as a generalized disturbance, which can be estimated and compensated in real time (Carreño Zagarra, 2020). This feature is particularly relevant in rehabilitation scenarios, where factors such as stiffness and spasticity introduce uncertainties that are difficult to model explicitly.

On the other hand, QFT-based robust control enables the design of controllers that meet performance specifications in the presence of parametric uncertainty and external disturbances (Houpis et al., 2006), (Garcia-Sanz, 2017a). In this framework, variations in patient conditions and system dynamics can be addressed within a structured uncertainty representation, allowing stability and performance to be guaranteed over a defined operating range.

This document is organized as follows: Chapter 2 presents the theoretical foundations required to understand the problem, including modeling principles and control strategies. Chapter 3 describes the development of the proposed solution, along with the implementation of the control strategies and the obtained results. Chapter 4 presents the conclusions derived from this work, while Chapter 5 outlines recommendations for future research. Finally, the appendices include complementary information related to the electronic design and implementation details.

1. Objectives

1.1 General Objective

To design and implement, at the laboratory prototype level, an advanced control strategy for the angular position of the fingers of a hand exoskeleton, in order to replicate the dynamics of a non-paretic hand.

1.2 Specific Objectives

To formulate a mathematical dynamic model of a hand exoskeleton that fits the prototype available in the laboratory, in order to represent the kinematic and dynamic behavior associated with the basic movements of a healthy hand.

To design an advanced control technique based on robust control strategies and active disturbance rejection, in order to satisfy the design parameters and dynamic conditions required to control flexion and extension movements of the paretic hand.

To numerically and experimentally validate the performance of the control system in terms of position and average velocity variables through tests that establish real therapy conditions, involuntary movements, and disturbances.

2. Theoretical Framework

2.1 Post-Stroke Rehabilitation Therapies

Upper limb rehabilitation in patients who have suffered a stroke requires a comprehensive approach and individualized intervention, since the recovery of motor function is variable and does not occur in the same way in all cases (Tran et al., 2021). Depending on the stage of recovery and the level of motor impairment, the therapeutic intervention is adapted with the objective of gradually restoring control and functionality of the limb.

In the initial stages, when the patient presents little or no voluntary control, assisted therapy is used, in which the movement is generated by the device following predefined trajectories. To guarantee safety, joint ranges are usually limited between 80–95

During each movement cycle, extension and flexion of the wrist and fingers contribute to the opening and closing function of the hand. Extension movements are generally the most affected, performed over variable ranges, with lower speed and impaired voluntary control, because the flexor musculature presents increased muscle tone, with the wrist and fingers in flexion, which limits hand opening (Norman et al., 2024). In the initial stages, movement cycles are usually on the order of 5 to 7 seconds, progressively increasing the speed and number of repetitions as the patient's motor capacity improves, maintaining short pauses to avoid fatigue. In more advanced stages, the system can incorporate modes where the patient actively participates in the movement, either through partial assistance or controlled resistance. In these cases, cycle times can increase (up to approximately 10–12 seconds) due to the greater muscular demand and the control required during human-device interaction (Singh et al., 2021).

2.2 Active Disturbance Rejection Control (ADRC)

Active Disturbance Rejection Control (ADRC) is a control strategy whose fundamental purpose is to improve the performance of dynamic systems in the presence of internal uncertainties and external disturbances. Unlike classical approaches that depend heavily on an accurate system model, ADRC adopts a more pragmatic perspective: it considers that all unknown dynamics, modeling errors, and disturbances can be grouped into a single "total disturbance," which is estimated and compensated in real time (Carreño Zagarra, 2020).

This idea introduces a relevant conceptual shift with respect to traditional schemes such as PID control or even conventional state-space formulations. Instead of focusing on detailed model identification, ADRC shifts the problem toward the active estimation of what is unknown about the system. To achieve this, it incorporates an extended state observer that not only reconstructs the state variables but also estimates the total disturbance as an additional system variable. This estimation allows the design of a control law that acts by actively canceling its effects, thus achieving more robust behavior against parametric variations, unmodeled dynamics, and external disturbances.

The fundamental idea of ADRC can be interpreted from the scheme shown in Figure 1, where the total disturbance is estimated through an extended state observer (ESO) and subsequently compensated in the control signal. Under this structure, the closed-loop system behaves approximately as a disturbance-free plant, provided that the estimation is sufficiently accurate.

Figure 1

ADRC control scheme

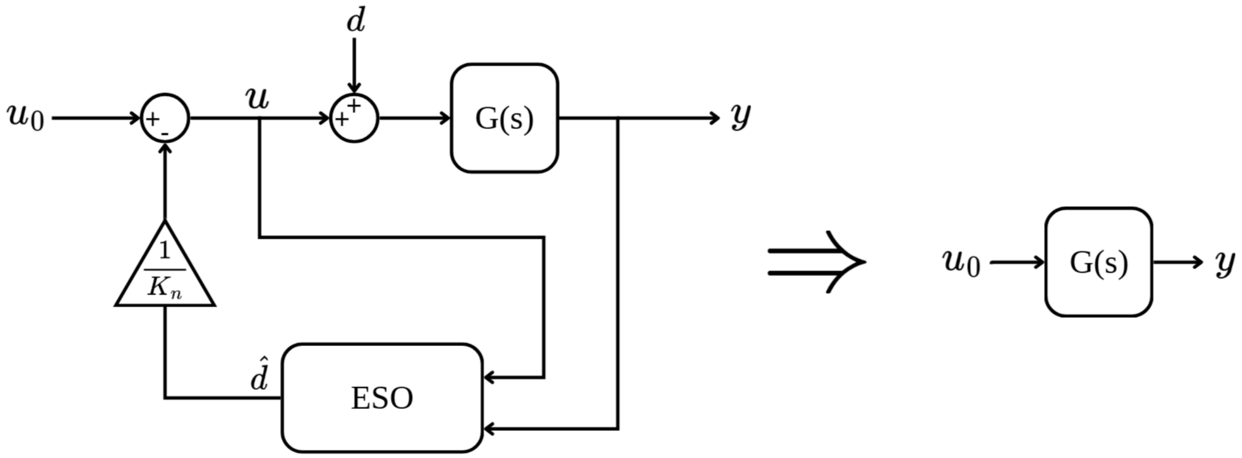

To formalize the idea of disturbance estimation and compensation, it is necessary to introduce the mathematical formulation on which the observer used in ADRC is based. In particular, a generalization of the extended state observer can be described by the so-called Generalized Proportional-Integral (GPI) observers (Carreño Zagarra, 2020), which allow the systematic estimation of higher-order disturbances. Consider a planar system of order n described by:

$$y^{(n)} = K(t, y)u + \psi(t)$$

where $K(t, y)$ is a known, bounded, and nonzero function, and $\psi(t)$ represents an unknown disturbance, which is assumed to be bounded along with its derivatives up to a certain finite order. This formulation groups both model uncertainties and external disturbances into a single term, consistent with the ADRC philosophy.

To estimate both the system states and the total disturbance, an observer of augmented order $n + m$ is used, where n corresponds to the order of the system and m defines the order of the disturbance to be estimated. The observer structure incorporates a chain of integrators that allows the reconstruction of higher-order unknown dynamics, expanding its estimation capability in the presence of complex disturbances. In particular, larger values of m allow capturing more elaborate variations in the disturbance, while the case $m = 1$ corresponds to the classical extended state observer (ESO) used in ADRC. The observer dynamics can be represented by the following set of equations:

$$\begin{aligned} \dot{\hat{x}}_j &= \hat{x}_{j+1} + \lambda_{m+n-j-1}(y - \hat{y}), \quad j = 0, \dots, n-2 \\ \dot{\hat{x}}_{n-1} &= K_n u + z_0 + \lambda_m (y - \hat{y}) \\ \dot{z}_l &= z_{l+1} + \lambda_{m-1}(y - \hat{y}), \quad l = 0, \dots, m-2 \\ \dot{z}_{m-1} &= \lambda_0 (y - \hat{y}) \end{aligned} \tag{2.1}$$

Where the vector of estimated states $\hat{x}$ represents the reconstruction of the system state, defined as

$$\hat{x} = \begin{bmatrix} \hat{x}_0 & \hat{x}_1 & \cdots & \hat{x}_{n-1} \end{bmatrix}^T,$$

in which $\hat{x}_0 = \hat{y}$ corresponds to the estimation of the output y, while $\hat{x}_1, \hat{x}_2, \ldots, \hat{x}_{n-1}$ represent respectively the derivatives $\dot{y}, \ddot{y}, \ldots, y^{(n-1)}$.

Similarly, the extended disturbance vector is defined as

$$z = \begin{bmatrix} z_1 & z_2 & \cdots & z_m \end{bmatrix}^T,$$

in which $z_0 = \hat{\psi}$ corresponds to the estimation of the disturbance ψ, while $z_1, z_2, \ldots, z_{m-1}$ represent respectively the derivatives $\dot{\hat{\psi}}, \ddot{\hat{\psi}}, \ldots, \hat{\psi}^{(m-1)}$.

The dynamics of the estimation error are governed by the choice of the observer gains $\{\lambda_0, \ldots, \lambda_{m+n-1}\}$, which are selected such that the associated characteristic polynomial is Hurwitz, thus guaranteeing convergence of the error:

$$p_{obs}(s) = s^{n+m} + \lambda_{n+m-1} s^{n+m-1} + \cdots + \lambda_0$$

Under this condition, the disturbance estimation error can be made arbitrarily small, allowing its effective compensation within the control law.

2.3 Robust Control

While strategies based on active estimation seek to compensate disturbances and unmodeled dynamics in real time, an alternative approach addresses the problem of variability from a preventive and structural perspective. This methodology is based on the design of a fixed-parameter controller capable of guaranteeing adequate system performance in the presence of a predefined set of variations, without requiring online adaptation (Garcia-Sanz, 2017b).

In applications involving direct human-machine interaction, such as rehabilitation exoskeletons, this approach is especially relevant, since the user's biomechanical parameters, such as limb mass or joint stiffness, are not constant but vary within bounded operating ranges (Tran et al., 2021).

To mathematically formalize this structural uncertainty, the concept of uncertainty is used, which is classified into two main categories. Structured or parametric uncertainty models variations in the known physical properties of the plant. In contrast, unstructured uncertainty groups unmodeled or high-frequency dynamics such as nonlinear effects, mechanical flexibilities, or delays, which are typically represented through bounds in the frequency domain (Spong et al., 2020).

This formulation allows the design of controllers capable of guaranteeing stability and performance within a set of models that represent the possible behavior of the system, laying the foundations for the use of robust design methodologies such as quantitative feedback theory (QFT).

2.4 Control Based on Quantitative Feedback Theory (QFT)

There are various methodologies for designing robust controllers, depending on the system characteristics and the nature of the uncertainties involved. One of them is Quantitative Feedback Theory (QFT) (Horowitz, 1991), which enables the design of robust controllers in the frequency domain while ensuring that performance specifications are met under parametric uncertainties. In this methodology, the plant is not represented by a single nominal model, but rather by a family of models that describes its variability. This set is analyzed in the frequency domain through plant templates, which show how the system magnitude and phase vary over different frequencies of interest.

One of the main advantages of QFT is that it explicitly incorporates model uncertainties, external disturbances, and measurement noise into the design process. For this purpose, specifications related to reference tracking, disturbance rejection, relative stability, and robustness are established and then translated into bounds on the Nichols chart (Houpis et al., 2006). The general control structure employed in QFT is shown in Figure 2. In this figure, r represents the desired reference, $F(s)$ corresponds to the prefilter used to improve reference tracking, $C(s)$ is the controller responsible for shaping the open-loop dynamics, and $P(s)$ represents the plant of the system.

Additionally, this configuration considers external signals that affect system performance: V denotes disturbances at the plant input, D denotes disturbances applied to the mechanical output, N denotes measurement noise present in the sensor, and $H(s)$ denotes the dynamics of the feedback element. This formulation enables a comprehensive analysis of the system behavior under real operating uncertainties and disturbances.

Figure 2

General control structure in QFT.

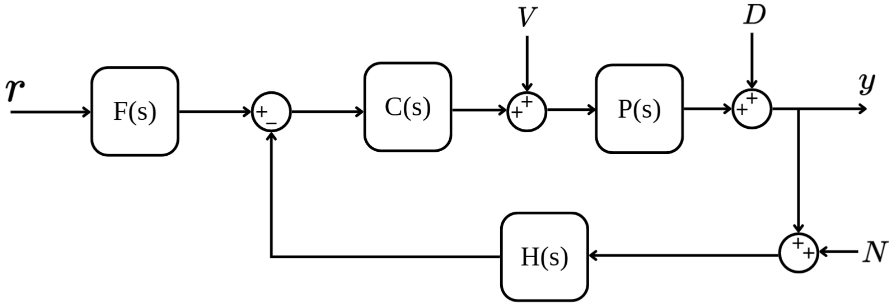

Under this paradigm, controller synthesis is formulated as a loop-shaping problem. The objective is to shape the nominal open-loop transfer function, defined as $L_0(s) = P_0(s)C(s)$, so that it strictly satisfies the imposed bounds, thereby ensuring robust performance. Consequently, the QFT design procedure is structured into the following fundamental stages (Garcia-Sanz, 2017a):

- **Frequency selection:** definition of the relevant frequencies for analyzing the system dynamics.
- **Uncertainty templates:** representation of the plant parametric variations on the Nichols chart for each selected frequency.
- **Performance specifications:** requirements related to tracking, disturbance rejection, and robustness.
- **Bounds construction:** generation of constraints on the Nichols chart derived from the specifications.
- **Loop-shaping:** controller design such that the nominal open-loop transfer function satisfies all established bounds.
- **Prefilter:** complementary adjustment of the transient response and reference tracking without modifying system robustness.

3. Solution Development

3.1 Mechanical System Description

The hand exoskeleton used in this project corresponds to a rigid-structure device, based on the mechanical design proposed in (Carreño Jerez et al., 2026). From this design, the fabrication, assembly, and implementation of the device were carried out. This system is externally attached to the back of the patient's hand and is designed to assist the flexion and extension movements of the fingers.

As shown in Figure 3, the device is composed of four main elements: (i) a dorsal structural base, (ii) guide rails, (iii) transmission links, and (iv) actuators.

Figure 3

Mechanical structure of the hand exoskeleton.

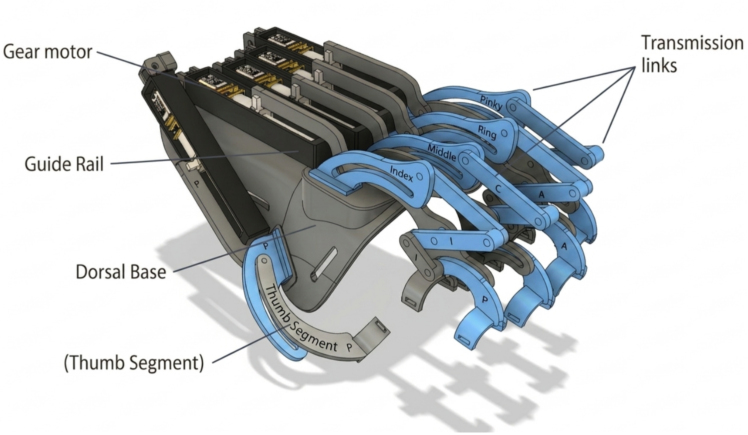

The dorsal base constitutes the main support of the system and serves as the fixation point to the back of the user's hand. On this base, the guide rails are arranged, which, together with a worm screw mechanism, allow transforming the rotational movement of the motor into a linear displacement.

This linear movement is subsequently transmitted to the linkage system, responsible for generating the joint movement of the fingers. Figure 4 illustrates the operating principle of the actuation mechanism. The actuators used correspond to geared motors with a maximum output speed of 500 rpm.

Figure 4

Linear actuation mechanism.

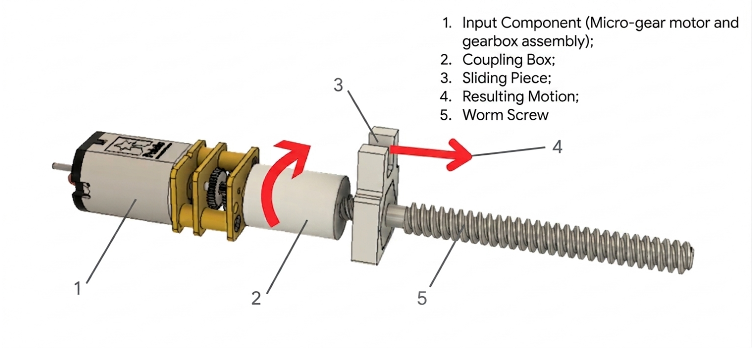

The linkage system transforms the linear displacement into rotational movement in the metacarpophalangeal (MCP) and proximal interphalangeal (PIP) joints of each finger. Due to the geometry of the mechanism, both joints are coupled, so the angle of the PIP joint depends on the angular position of the MCP joint. Consequently, each finger presents a single degree of freedom. The range of joint motion achieved in the MCP joint is approximately between 6.66° in maximum extension and 40° in maximum flexion.

3.2 Electronic System Description

The electronic instrumentation of the exoskeleton was designed with the objective of implementing actuation, signal acquisition, and execution of the control strategy. For this purpose, a system composed of four main elements was developed and implemented: (i) a microcontroller, (ii) motor drivers, (iii) an optical distance sensor, and (iv) a printed circuit board (PCB) that integrates the previous components.

Figure 5 shows the block diagram of the electronic system and its interaction with the exoskeleton.

Figure 5

Block diagram of the electronic control system of the exoskeleton.

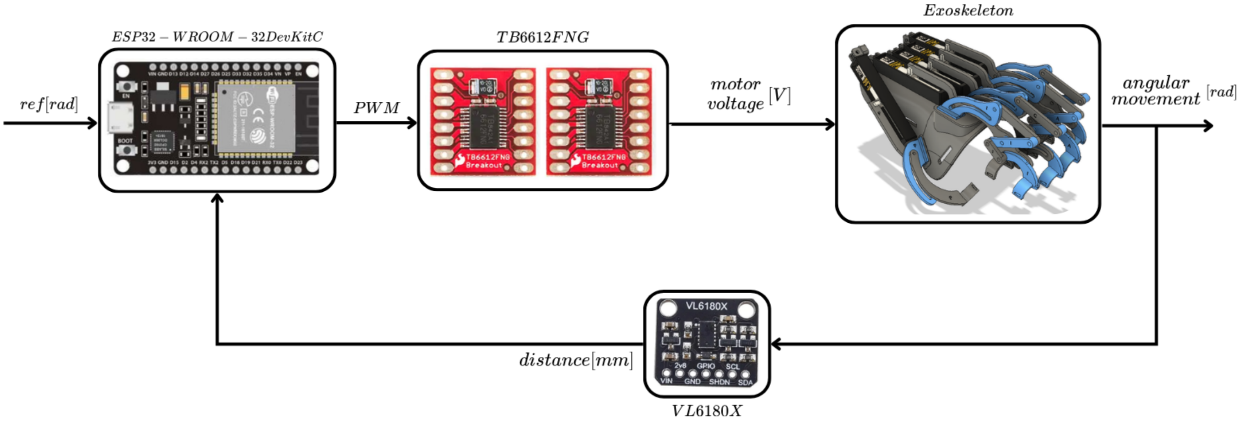

The core of the system is the ESP32-WROOM-32 DevKitC microcontroller. This device fulfills two main functions: first, it generates the PWM signals that are sent to the motor drivers to regulate the voltage applied to the actuators; second, it manages communication through the I2C protocol with the optical sensor, allowing continuous acquisition of the position variable. This microcontroller was selected for its processing capability, integrated connectivity, and low cost, which makes it a widely used solution in embedded systems.

For actuation, two TB6612FNG motor drivers are used, each capable of independently driving two DC motors. This configuration allows controlling the four active fingers of the exoskeleton, keeping the thumb in a fixed position. These drivers were chosen due to their availability in the market, ease of integration, and electrical specifications suitable for the application, as well as their dual-channel architecture, which allows reducing the number of required components and optimizing the space occupied on the PCB.

Finally, system feedback is obtained through a VL6180X optical distance sensor, located on the index finger, above the motor and behind the mechanism responsible for generating linear displacement. This sensor measures the distance x corresponding to the displacement of the actuating piece, from which the angular position of the metacarpophalangeal joint θ_1 is calculated using the kinematic relationship described in equation (3.1).

The use of a single sensor is sufficient, since under ideal conditions the fingers present a coupled motion during flexion and extension actions, which allows inferring the state of the system from a single measurement, thus reducing system complexity and associated costs. The VL6180X sensor was selected for its accuracy in short-distance measurements, robustness under lighting conditions, and relatively low cost.

All electronic components are integrated into a PCB with a modular architecture, using pin headers that facilitate experimental development and allow component replacement in case of failure. The schematic and layout design, together with the criteria for selecting trace widths and other design considerations, are presented in **Appendix E**.

3.3 System Modeling and Identification

3.3.1 Kinematic and Dynamic Model Based on Physical Principles

In order to describe the mechanical behavior of the exoskeleton, the kinematic relationship between the linear displacement produced by the actuators and the resulting angular motion in the joints is established. This relationship is obtained by assuming that the motion of the contact point follows a circular trajectory of constant radius r_1, neglecting effects such as mechanical clearances and system deformations.

As shown in Figure 6, this relationship can be approximated as proportional and is described by the following expression:

$$x = r_1 \theta_1 \tag{3.1}$$

where x corresponds to the linear displacement of the actuating piece with respect to a reference position, r_1 is the effective radius associated with the semicircular groove trajectory, and θ is the angle described along this trajectory, being equal to the rotation angle θ_1.

Geometrically, θ_1 coincides with the rotation of the metacarpophalangeal (MCP) joint of the exoskeleton, measured with respect to an angular reference defined in the finger extension configuration.

Figure 6

Kinematic relationship.

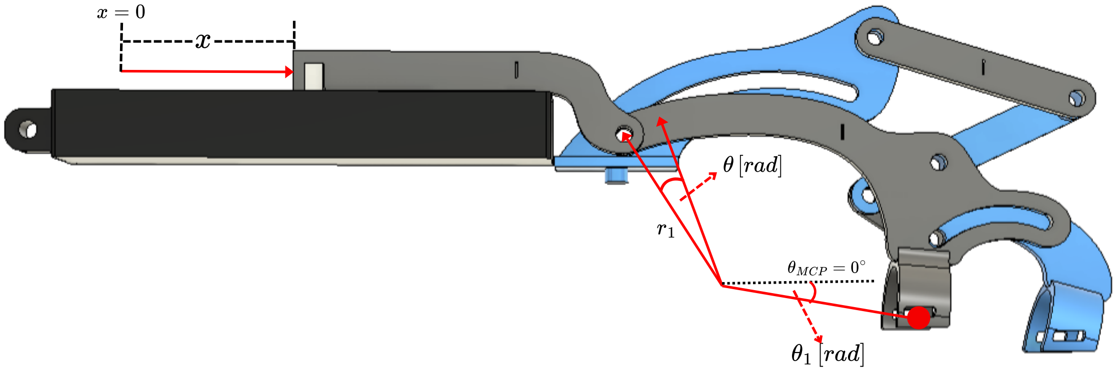

With the established kinematic relationship, it is possible to formulate the dynamic model of the system based on the forces and torques acting on the mechanism. To do this, the Newton–Euler approach is applied at the joints of the linkage system. Since each finger has a single degree of freedom, the dynamics of the metacarpophalangeal (MCP) and proximal interphalangeal (PIP) joints are coupled through the kinematic constraint imposed by the geometry of the mechanism.

Figure 7 shows the free-body diagram of the system, where the relevant forces and torques that will be considered in the formulation of the dynamic model are identified.

Figure 7

Force diagram.

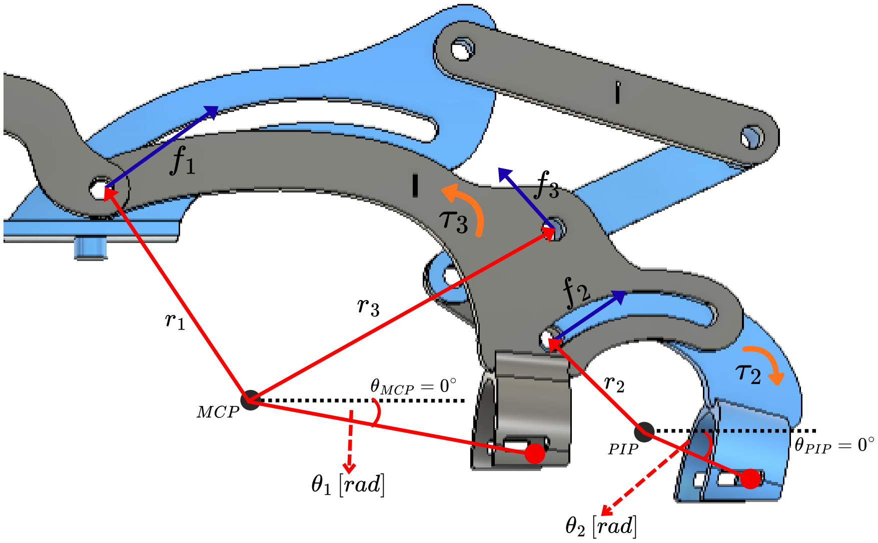

Applying Newton–Euler to each joint separately, the following equations of motion are obtained:

$$f_1 \cdot r_1 - \tau_3 - k_1 \cdot \dot{\theta}_1 = J_1 \cdot \ddot{\theta}_1 \tag{3.2}$$

$$\tau_2 - k_2 \cdot \dot{\theta}_2 = J_2 \cdot \ddot{\theta}_2 \tag{3.3}$$

where J_1 and J_2 are the equivalent moments of inertia of each joint, k_1 and k_2 are the viscous friction coefficients at the MCP and PIP joints, respectively, and τ_2 and τ_3 are the interaction torques between the components responsible for joint motion, related to the internal forces of the mechanism by:

$$\tau_2 = f_2 \cdot r_2, \qquad \tau_3 = f_3 \cdot r_3 \tag{3.4}$$

Since the geometry of the linkage mechanism couples both joints, the virtual power condition $\tau_3 \cdot \dot{\theta}_1 = \tau_2 \cdot \dot{\theta}_2$ holds, and it is additionally assumed that the internal interaction forces are equal, that is, $f_2 = f_3$.

Under these conditions, the kinematic constraint between joints is expressed as:

$$\dot{\theta}_2 = \frac{r_3}{r_2} \cdot \dot{\theta}_1 \implies \ddot{\theta}_2 = \frac{r_3}{r_2} \cdot \ddot{\theta}_1 \tag{3.5}$$

This relationship confirms that the angular position of the PIP joint is completely determined by the position of the MCP joint, which is consistent with the single degree of freedom of the system.

Isolating f_3 from equation (3.2) and equating it with the expression $f_2 = f_3$ obtained from equation (3.3):

$$f_3 = \frac{f_1 \cdot r_1 - k_1 \cdot \dot{\theta}_1 - J_1 \cdot \ddot{\theta}_1}{r_3} \tag{3.6}$$

$$f_2 = f_3 = \frac{k_2 \cdot \dot{\theta}_2 + J_2 \cdot \ddot{\theta}_2}{r_2} \tag{3.7}$$

Equating (3.6) and (3.7), and substituting the kinematic constraint (3.5), we obtain:

$$\left(\frac{-J_1}{r_3} + \frac{J_2 \cdot r_3}{r_2 \cdot r_2}\right) \ddot{\theta}_1 + \left(\frac{k_1}{r_3} + \frac{k_2 \cdot r_3}{r_2 \cdot r_2}\right) \dot{\theta}_1 = f_1 \cdot \frac{r_1}{r_3} \tag{3.8}$$

Grouping the terms into equivalent parameters, the unified equation of motion of the system is obtained:

$$J\ddot{\theta}_1 + k\dot{\theta}_1 = f_1 r \tag{3.9}$$

Since the electrical time constant of the motor is significantly smaller than the mechanical time constant of the mechanism, the electrical dynamics of the motor can be neglected. Under this assumption, the relationship between the force exerted by the actuator f_1 and the input voltage v can be approximated as a constant b_f, so that the dynamic model of the system is expressed as:

$$J_f\ddot{\theta}_1 + k_f\dot{\theta}_1 = b_f v \tag{3.10}$$

This expression constitutes the differential equation that represents the dynamics of the system.

3.3.2 Model parameters and identification formulation

The identification problem consists of finding the values of $\boldsymbol{\rho} = [J_f,\ k_f,\ b_f]^T$ that minimize the error between the simulated angular response of the model and the experimentally measured angular response to the same input signal $v(t)$. This problem is solved using the `tfest` function from the *System Identification Toolbox* of MATLAB, which allows estimating continuous-time transfer functions from experimental input and output data.

To obtain the required data, an identification experiment was designed on the exoskeleton. In this experiment, a voltage excitation signal was applied to the motor that controlled the actuation mechanism of the index finger, in order to record the angular response of the MCP joint.

The input signal was generated from a PWM sequence established by the microcontroller, which switched the motor controller between three states: maximum operating voltage (corresponding to a 100% duty cycle) to excite the flexion movement, zero voltage as a resting state, and reverse voltage to excite the extension movement.

The experiment was performed for six operating voltage levels: 2, 4, 6, 8, 10 and 12 V. For each level, the flexion and extension times were adjusted so that the movement was executed approximately over the full range of motion of the joint, while the resting intervals ensured that the exoskeleton started from a stable state at the beginning of each cycle. Since two identifications are performed per voltage level, one for the flexion cycle and another for the extension cycle, a set of models with the following form is obtained:

$$G_i(s) = \frac{K_i}{s\,(s + p_i)}, \quad i = 1, 2, \ldots, 12 \tag{3.11}$$

From this set, a nominal plant is obtained by averaging the identified parameters:

$$G_{nom}(s) = \frac{\bar{K}}{s\,(s + \bar{p})} \tag{3.12}$$

where $\bar{K}$ and $\bar{p}$ correspond to the arithmetic mean of the identified gains and poles, respectively. This set of individual models will also be used in the design of the QFT controller to characterize the parametric uncertainty of the system.

3.3.3 Acquisition and processing of experimental data

The output signal $\theta_1(t)$ was obtained from the measurements of the VL6180X optical distance sensor, which records the linear displacement x of the actuator with a sampling period of $T_s = 30$ ms. From this measurement, the microcontroller calculates the angular position of the MCP joint using the kinematic relationship described in equation (3.1), and transmits the data to the computer through the Arduino serial monitor, from where they were exported and stored in a plain text file (`.txt`). This file contains both the input voltage signal $v(t)$ and the calculated angular position $\theta_1(t)$, recorded synchronously at the same sampling period. The code implemented in the microcontroller to perform this task is presented in **Appendix A**.

Since each experiment includes a flexion cycle followed by an extension cycle, a MATLAB script was developed to process the recorded data file and automatically divide it into two independent files: one corresponding to the flexion cycle and the other to the extension cycle. This separation allows independent identification for each direction of motion, thus obtaining two models for each evaluated voltage level.

This procedure was carried out under two operating conditions: without load, corresponding to the exoskeleton operating without a hand, and with load, corresponding to the exoskeleton with the user's hand placed. This distinction allows characterizing the variation in the system dynamics under changes in mechanical load.

During the experiment, the presence of a dead time in the system response was identified: when voltage was applied to the motors, the mechanism took approximately 300 ms to start moving due to the mechanical characteristics of the exoskeleton, particularly the static friction of the worm gear. This delay was consistently observed and independent of the applied voltage level, and constitutes an intrinsic characteristic of the system that must be considered when evaluating the performance of the implemented control strategy.

3.3.4 Model identification

Model identification was carried out using the `tfest` function from the *System Identification Toolbox* of MATLAB, using the voltage signals $v(t)$ and joint angle $\theta_1(t)$ obtained in the experimental acquisition.

The goal was to estimate a transfer function consistent with the structure of the model derived in equation (3.10), whose canonical form corresponds to a cascaded integrator with a real pole:

$$G(s) = \frac{\Theta_1(s)}{V(s)} = \frac{b_f/J_f}{s\left(s + k_f/J_f\right)} \tag{3.13}$$

Since $G(s)$ contains an integrator, an approach was adopted that incorporates this structural knowledge directly into the identification process. Rewriting $G(s)$ as:

$$G(s) = \frac{\tilde{G}(s)}{s}, \qquad \tilde{G}(s) = \frac{\Theta_1(s)}{\tilde{V}(s)} \tag{3.14}$$

where $\tilde{V}(s) = V(s)/s$ corresponds to the integral of the input signal. In this way, it is possible to directly identify $\tilde{G}(s)$ as a first-order transfer function without an integrator, using $\tilde{v}(t)$ as input and $\theta_1(t)$ as output. The complete transfer function is then recovered as:

$$G(s) = \frac{\tilde{G}(s)}{s} \tag{3.15}$$

This procedure was systematically applied by looping over all available files, independently processing the flexion and extension data for each of the six voltage levels evaluated (2, 4, 6, 8, 10, and 12 V), which resulted in a set of 12 individual transfer functions. From this set, the nominal plant was obtained by averaging the identified parameters:

$$G_{nom}(s) = \frac{\bar{K}}{s\,(s + \bar{p})} \tag{3.16}$$

where $\bar{K}$ and $\bar{p}$ correspond to the arithmetic mean of the gains and poles identified, respectively, within the set of obtained models.

3.3.5 Identification Results

As a result of the identification process, a set of 24 transfer functions was obtained, corresponding to the flexion and extension cycles for each of the six voltage levels evaluated, under two operating conditions: no load (exoskeleton without hand) and with load (exoskeleton with hand). All the identified models presented a fit percentage greater than 90%, which validates the capability of the adopted approach to represent the system dynamics under both conditions. Table 1 summarizes the parameters obtained in each identification.

Table 1

Parameters identified by load condition.

No load

V [V]	Mov.	K	p
2	Flex.	0.001325	0.08314
2	Ext.	0.004928	0.2374
4	Flex.	0.0007828	0.07028
4	Ext.	0.005325	0.4738
6	Flex.	0.00132	0.08956
6	Ext.	0.01009	0.8792
8	Flex.	0.001716	0.1214
8	Ext.	0.009034	0.8114
10	Flex.	0.002127	0.1613
10	Ext.	0.00969	0.808
12	Flex.	0.002615	0.1718
12	Ext.	0.01	0.8263

With load

V [V]	Mov.	K	p
2	Flex.	0.0003122	0.02452
2	Ext.	0.002552	0.2794
4	Flex.	0.000692	0.05302
4	Ext.	0.01225	1.144
6	Flex.	0.0009876	0.08392
6	Ext.	0.04729	4.396
8	Flex.	0.001514	0.09355
8	Ext.	0.08081	6.783
10	Flex.	0.001514	0.09355
10	Ext.	0.08081	6.783
12	Flex.	0.002582	0.1213
12	Ext.	0.03558	3.58

From the average of the parameters of both sets of models, the nominal plant of the system was obtained:

$$G_{nom}(s) = \frac{0.01358}{s\,(s + 1.174)} \tag{3.17}$$

This transfer function constitutes the nominal model used for the design of the control strategies described in the following sections.

The complete set of individual models obtained under both load conditions will also be used to characterize the parametric uncertainty of the system in the design of the QFT controller.

Additionally, the system transport delay was estimated, defined as the time elapsed between the application of voltage to the motors and the start of the mechanism movement. This delay was approximately 300 ms, so the complete transfer function can be represented as:

$$G(s) = \frac{0.01358}{s\,(s + 1.174)} e^{-0.3s} \tag{3.18}$$

However, the model without delay was used for the controller design in order to simplify the design and analysis process, considering that the delay is relatively small compared to the dominant system dynamics and that its effects are partially compensated by the controller action.

3.4 Design and Implementation of the ADRC Controller

3.4.1 System Model for Controller Design

To formulate the problem within the ADRC framework, it is convenient to express the system dynamics in the time domain using a differential equation. From the transfer function (3.17), we obtain:

$$\ddot{\theta}_1(t) + 1.174\dot{\theta}_1(t) = 0.01358\, v(t) \tag{3.19}$$

This equation describes the nominal behavior of the system. However, under real-world conditions, deviations from this model arise due to parameter uncertainties and external disturbances.

To incorporate these effects, the system dynamics are rewritten by separating the nominal model from the uncertainties:

$$\ddot{\theta}_1(t) = -a\,\dot{\theta}_1(t) + b\,v(t) + \psi(t) \tag{3.20}$$

where:

$$a = 1.174, \quad b = 0.01358 \tag{3.21}$$

and $\psi(t)$ represents the *total disturbance*.

Unlike other ADRC formulations, in which all non-integrating dynamics are grouped within the disturbance term, in this implementation the term associated with the velocity $-a\dot{\theta}_1(t)$ is explicitly retained. This decision is not arbitrary, but rather motivated by practical implementation considerations: it avoids completely shifting these dynamics to the observer in the form of a disturbance due to the physical limitations of the actuators. Indeed, including all the dynamics within the disturbance term can lead to more aggressive estimates and, consequently, control signals of higher magnitude. This effect is particularly relevant in systems with constraints on the control signal amplitude, where saturation becomes a critical issue. This aspect will be analyzed in greater detail in the controller implementation section.

Thus, the total disturbance is defined as:

$$\psi(t) = \Delta a\,\dot{\theta}_1(t) + \Delta b\,v(t) + d(t) \tag{3.22}$$

where:

- $\Delta a\,\dot{\theta}_1(t)$ represents the uncertainty in the coefficient associated with the system dynamics.
- $\Delta b\,v(t)$ models errors in the input gain.
- $d(t)$ corresponds to unmodeled external disturbances, such as variable friction, noise, and unaccounted mechanical interactions, as well as the interaction forces between the user and

the exoskeleton.

In the context of the proposed rehabilitation system, the term $d(t)$ becomes particularly relevant, as it incorporates the forces generated by patients with neuromotor conditions, such as those resulting from a stroke. These forces represent a significant source of uncertainty in the system dynamics, as they vary between patients and even during a single therapeutic session. Consequently, one of the fundamental objectives of the controller is to estimate and actively compensate for these effects, allowing the exoskeleton to assist and guide movement appropriately without being adversely affected by such interactions.

Finally, the system can be represented in state-space form as:

$$\begin{aligned} \dot{x}_0(t) &= x_1(t) \\ \dot{x}_1(t) &= -ax_1(t) + bv(t) + \psi(t) \\ y(t) &= x_0(t) \end{aligned} \tag{3.23}$$

where $x_0(t) = \theta_1(t)$ and $x_1(t) = \dot{\theta}_1(t)$.

This representation forms the basis for the design of the extended state observer, which will allow the total disturbance $\psi(t)$ to be estimated together with the system states, enabling its active compensation within the control law.

3.4.2 Design of the Extended State Observer (ESO)

The design of the Extended State Observer (ESO) is based on the generalized system presented in the theoretical framework in 2.1. In this work, an augmented-order structure is adopted, with two states associated with the physical system and two additional states intended for estimating the total disturbance and its dynamics.

The observer's estimated state vector is defined as:

$$\hat{x} = \begin{bmatrix} \hat{\theta}_1 & \hat{\dot{\theta}}_1 & \hat{\psi} & \hat{\dot{\psi}} \end{bmatrix}^T$$

where $\hat{\theta}_1$ and $\hat{\dot{\theta}}_1$ correspond to the estimated states of the original system, while $\hat{\psi}$ and $\hat{\dot{\psi}}$ represent the estimated total disturbance and its derivative, respectively. In this implementation, $m = 2$ is adopted, which implies modeling the total disturbance as a signal whose second derivative is bounded. This choice is not arbitrary, but rather reflects a trade-off between modeling capability and robustness against noise. An order of $m = 1$ (constant disturbance) would be insufficient to capture gradual variations in human-exoskeleton interaction, while a higher order would unnecessarily increase the observer's sensitivity to measurement noise and computational complexity. In particular, by considering $m = 2$, the observer is capable of tracking ramp-type disturbances, allowing for an adequate representation of progressive changes in interaction forces, variabe friction, and the user's biomechanical effects. Since in this application such disturbances do not exhibit abrupt variations but instead evolve relatively smoothly over time, this order is sufficient to capture them without amplifying high-frequency components associated with noise.

Under this formulation, the extended state observer can be written as:

$$\dot{\hat{x}}(t) = A\hat{x}(t) + Bv(t) + \lambda\big(y(t) - \hat{y}(t)\big), \quad \hat{y}(t) = C\hat{x}(t) \tag{3.24}$$

where the observer matrices are:

$$A = \begin{bmatrix} 0 & 1 & 0 & 0 \\ 0 & -1.174 & 1 & 0 \\ 0 & 0 & 0 & 1 \\ 0 & 0 & 0 & 0 \end{bmatrix}, \quad B = \begin{bmatrix} 0 \\ 0.01358 \\ 0 \\ 0 \end{bmatrix}, \quad C = \begin{bmatrix} 1 & 0 & 0 & 0 \end{bmatrix}$$

In this representation, the nominal plant dynamics are explicitly incorporated into the second state through the terms $-a_0\dot{\theta}_1(t)$ and $b_0v(t)$, in accordance with the formulation presented in (3.20).

For its digital implementation, the observer was discretized using a zero-order hold (ZOH), considering a sampling time of $T_s = 0.03\ s$. This value is selected as a trade-off between estimation accuracy and the system's processing capacity. In particular, the sensor requires preprocessing based on filtering, averaging, and median filtering, which introduces an effective delay that must be compensated for by a sufficiently high sampling frequency to adequately capture the system dynamics.

Under this discretization, the observer takes the form:

$$\hat{x}(k+1) = \Phi\hat{x}(k) + \Gamma v(k) + \lambda_p\big(y(k) - \hat{y}(k)\big), \quad \hat{y}(k) = H\hat{x}(k) \tag{3.25}$$

where the matrices of the discrete extended state observer are:

$$\Phi = \begin{bmatrix} 1.0000 & 0.0295 & 0.0004 & 0.0000 \\ 0 & 0.9654 & 0.0295 & 0.0004 \\ 0 & 0 & 1.0000 & 0.0300 \\ 0 & 0 & 0 & 1.0000 \end{bmatrix} \quad \Gamma = \begin{bmatrix} 6.0399 \times 10^{-6} \\ 4.0031 \times 10^{-4} \\ 0 \\ 0 \end{bmatrix} \quad H = \begin{bmatrix} 1 & 0 & 0 & 0 \end{bmatrix}$$

This structure corresponds to a discrete-time predictive observer, which allows the state at time $k+1$ to be estimated directly. This feature is fundamental for real-time implementation, as it avoids the inherent delay associated with estimation based solely on time k, enabling a more anticipatory control action and reducing the lag between estimation and system correction.

The observer gains λ_p are obtained using the pole placement method with MATLAB's `place` command. In the continuous-time case, this procedure is equivalent to selecting coefficients that ensure a Hurwitz characteristic polynomial, but applied directly to the discrete matrix Φ. In this case, the observer poles are located around $s = -4$, as they represent dynamics approximately 3.5 times faster than the nominal system dynamics. This ensures rapid convergence of the estimation error without excessively amplifying measurement noise by increasing the observer bandwidth too much.

The discrete poles selected for the observer are defined as:

$$z = e^{-4T_s} - \Delta z, \quad T_s = 0.03, \quad \Delta z = \begin{bmatrix} 0.0001 & 0.001 & 0.005 & 0.008 \end{bmatrix}$$

The small separation between poles is introduced as a numerical requirement of the assignment algorithm, avoiding collinearity issues and improving the numerical conditioning of the design.

From these poles, the discrete-time observer gains λ_p are obtained:

$$\lambda_p = \begin{bmatrix} 0.4318 \\ 2.1539 \\ 6.9565 \\ 6.9580 \end{bmatrix} \tag{3.26}$$

3.4.3 Design of the Control Law

The implemented control law is based on a state feedback structure supplemented by active cancellation of the disturbance estimated by the extended state observer. In particular, the following expression is adopted:

$$u(t) = K_r\,\theta_{ref}(t) - \left(k_0 x_0 + k_1 x_1 + k_2 \hat{\psi}\right) \tag{3.27}$$

where $\theta_{ref}(t)$ is the reference signal, $x_0 = \theta, x_1 = \dot{\theta}$ are the system states, and $\hat{\psi}$ corresponds to the estimated total disturbance. The control signal $u(t)$ is equivalent to the voltage applied to the actuator.

In this formulation, the terms k_0 and k_1 correspond to state feedback, while k_2 acts on the estimated disturbance term $\hat{\psi}$, allowing its effect on the system dynamics to be attenuated. As a result, the closed-loop behavior is primarily governed by the nominal model described in (3.23). Under this approximation, the closed-loop poles are placed with the aim of meeting time-domain performance specifications.

The design specifications were defined based on a settling time of $8\,s$ and an overshoot of 1%. These conditions reflect practical criteria associated with the application: on the one hand, the settling time is selected in accordance with the duration of therapeutic movements, while the low overshoot aims to prevent overextensions that could compromise user safety.

From these specifications, the desired poles in the continuous domain are obtained:

$$s_{1,2} = -0.5000 \pm 0.3411i$$

Subsequently, these poles are transformed to the discrete domain using the relation:

$$z = e^{sT_s}$$

resulting in:

$$z_{1,2} = 0.9851 \pm 0.0101i$$

Based on these poles, the state feedback gains are calculated via pole placement using the MATLAB `place` command:

$$k_0 = 27.0462, \quad k_1 = -12.2183$$

Furthermore, the gain associated with disturbance compensation is defined as the inverse of the input gain of the nominal model in order to achieve approximate disturbance cancellation:

$$k_2 = \frac{1}{b} = \frac{1}{0.01358} = 73.6377$$

Finally, to ensure adequate reference tracking in steady state, a feedforward gain K_r is introduced, which was tuned via simulation to correct the system's static gain:

$$K_r = 27.049 \tag{3.28}$$

3.4.4 Simulation of the ADRC Controller

To evaluate the performance of the designed ADRC controller, simulations were carried out to analyze both reference tracking capability and disturbance rejection. The simulation files are presented in **Appendix F**.

The reference signal is given by:

$$\theta_{\text{ref}}(t) = \begin{cases} \frac{5}{43} + \frac{20}{43}\frac{t}{10} & 0 \leq t < 10 \\ \frac{25}{43} & 10 \leq t < 20 \\ \frac{25}{43} - \frac{20}{43}\frac{t-20}{10} & 20 \leq t < 30 \\ \frac{5}{43} & 30 \leq t < 40 \end{cases}$$

This signal is defined over the interval $t \in [0, 40]$ and repeats periodically, generating a trapezoidal profile that alternates between low and high levels with linear transitions. It should be noted that the values 5 and 25 correspond to distances in millimeters measured by the system sensor. These values are scaled using equation 3.1 to map linear displacement to angular position. This signal is shown in Figure 16.

This type of signal allows emulation of repetitive trajectories used in hand rehabilitation therapies, as discussed in the theoretical framework.

Figure 16 shows the system response to the reference signal, along with the applied control signal. This simulation was carried out by introducing a ramp-type disturbance $\psi(t)$ with a slope of 10^{-3}, in order to simultaneously evaluate tracking performance and disturbance rejection. The controller achieves adequate tracking of the desired trajectory, exhibiting smooth behavior and no significant overshoot. However, a slight tracking delay is observed, which is consistent with the design specifications established for the control law, particularly the settling time of $T_s = 8\,s$ and the low allowed overshoot. These conditions imply dynamics that prioritize smoothness and safety of motion over response speed.

Figure 8

Reference tracking and control signal

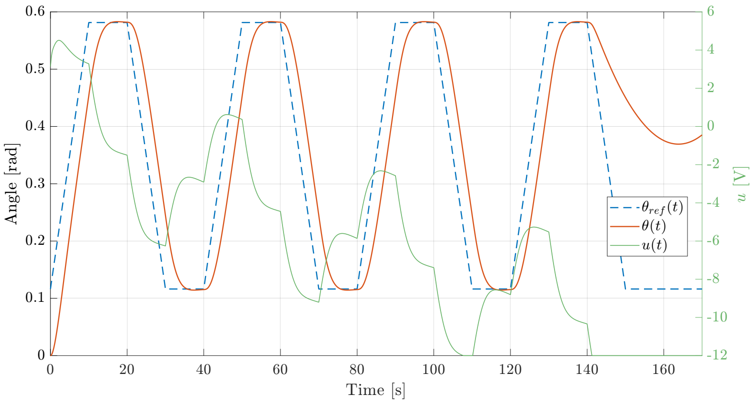

Figure 9 shows the relationship between the control signal $u(t)$ and the applied disturbance $\psi(t)$. It can be observed that the controller effectively compensates for the disturbance, demonstrating near-complete rejection. In particular, the control signal exhibits a slope similar to the disturbance, reflecting the action of the observer and the control law in estimating and actively canceling $\psi(t)$.

Figure 9

Control signal and applied disturbance

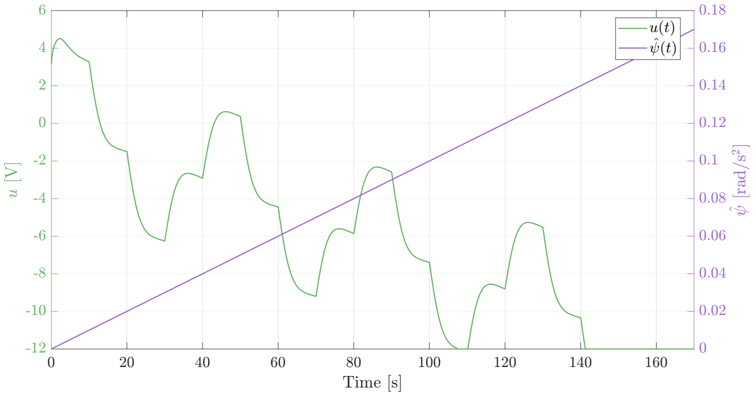

However, this behavior holds only within the physical limits of the system. In the implementation under consideration, the control signal u is restricted to the range $[-12, 12]$ V, corresponding to the maximum voltage allowed by the exoskeleton actuators. Once the control signal reaches these limits, saturation occurs, which prevents further compensation of the disturbance growth ψ.

As a result, the system loses its disturbance rejection capability in this operating region, leading to a deterioration in reference tracking θ_{ref}. This phenomenon highlights a significant practical limitation of the controller, stemming not from its theoretical design but from the physical constraints of the system.

3.4.5 Implementation of the ADRC Controller

The ADRC controller was implemented using an ESP32 microcontroller, which executes both the discrete extended state observer and the state-feedback control law in real time. The system was configured with a sampling period of $T_s = 0.03\,s$, in accordance with the previously established design.

The code was developed in the Arduino environment using the `BasicLinearAlgebra.h` library to facilitate the matrix operations required by the observer. The complete implementation code is presented in **Appendix D**.

During each sampling period, the system follows a structured processing sequence consisting of several stages. First, the signal from the `VL6180X` distance sensor is acquired. Due to the observer's sensitivity to noise, this signal undergoes a filtering process that combines median, moving-average, and exponential filtering, with the aim of attenuating high-frequency components and reducing measurement variability.

Next, the filtered signal is processed by the extended state observer, which estimates both the system states and the total disturbance according to the discrete model presented in (3.25). This yields an internal representation of the system that includes both the nominal dynamics and unmodeled effects.

In parallel, a trapezoidal reference signal is generated periodically, replicating the flexion-extension profile defined in the simulation stage. This reference is used together with the estimated states to compute the control signal using the law defined in 3.27.

Finally, the control signal is conditioned and applied to the actuator using PWM, while respecting the system's physical limitations, particularly the voltage range allowed by the motor. Additionally, a dead-zone compensation of approximately 1 V was incorporated, determined experimentally, as voltages below this threshold do not produce effective motor actuation.

One of the most critical aspects during implementation was the handling of measurement noise. Since ADRC treats all unmodeled dynamics as disturbances, any noise present in the sensor is directly reflected in the estimate of $\hat{\psi}$, affecting the control signal. For this reason, the input signal filtering scheme was carefully designed.

Additionally, the function `filtro2()` was incorporated, implementing a second-order Butterworth digital filter with a cutoff frequency of approximately 1 Hz. This filter is applied to the disturbance estimated by the observer in order to eliminate high-frequency components that lack physical significance in the system dynamics. The selection of this cutoff frequency was based on spectral analysis of the disturbance signal, where it was observed that the dominant components lie below 1 Hz, while higher-frequency components correspond mainly to measurement noise.

On the other hand, as observed in simulation, the main limitation of the system is associated with saturation of the control signal due to the motor's physical voltage limits (-12 to 12 V). In this context, it was necessary to adjust the controller gains relative to their theoretical values in order to avoid persistent saturation.

The final implemented gains were:

$$K = \begin{bmatrix} 34 & -15 & 20 \end{bmatrix}, \quad K_r = 34 \tag{3.29}$$

The main adjustment was made to the disturbance-related term (k_2), as the disturbance estimated in practice was found to be significantly larger than that predicted in simulation. Consequently, the controller's compensation capacity was reduced, preventing the control signal from remaining in continuous saturation.

3.4.6 Results of the ADRC Controller

The designed ADRC controller was experimentally evaluated under three different scenarios: two users with distinct dynamic characteristics and a no-load operating condition. This approach allows evaluation of the system's behavior under variations in mechanical interaction due to different load levels and usage conditions.

Figure 10

Results of the ADRC controller for User 1.

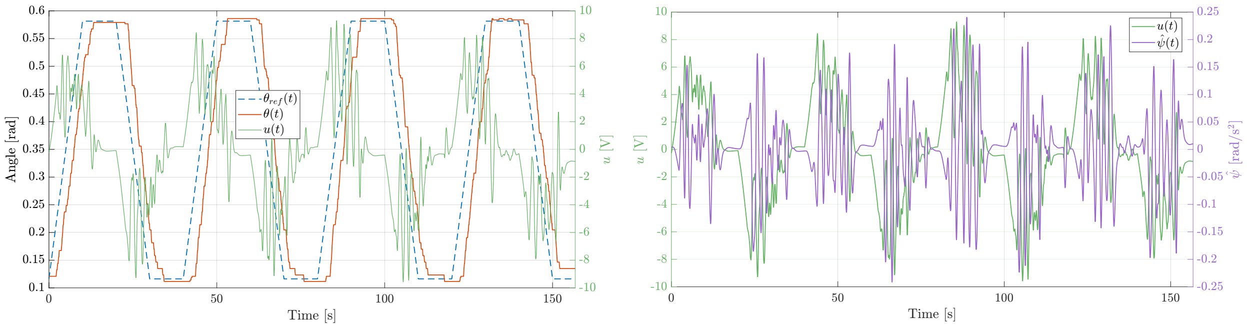

Figure 11

Results of the ADRC controller for User 2.

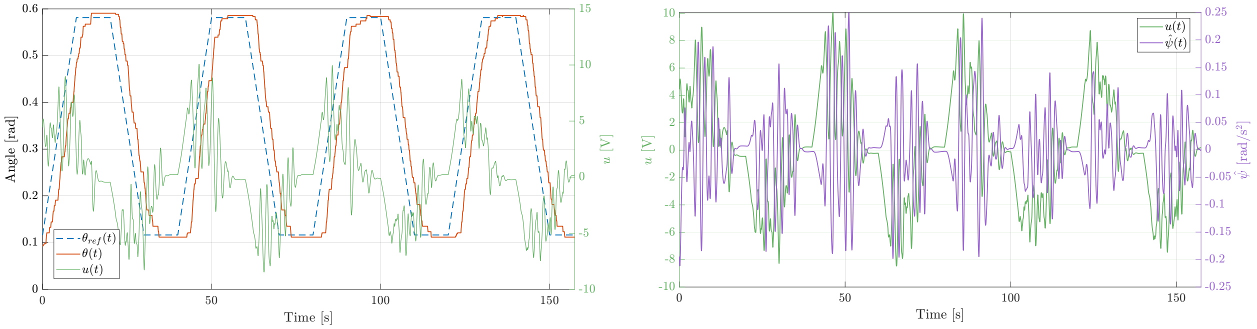

Figure 10 presents the results for User 1, Figure 11 shows the results for User 2, and Figure 12 illustrates the system behavior in the no-load condition.

Figure 12

Results of the ADRC controller in the no-load condition.

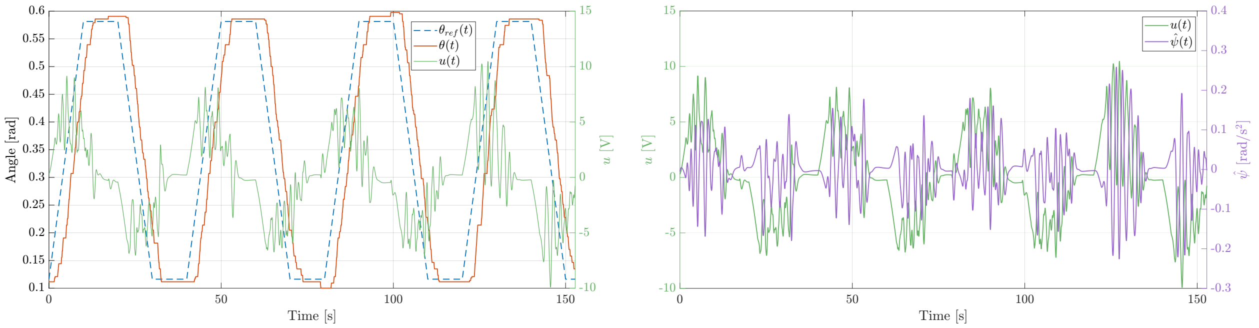

3.5 Design and Implementation of the QFT Controller

The design of the QFT controller requires a rigorous formulation based on the system dynamics. This analysis maps the physical and clinical requirements of the exoskeleton into formal mathematical constraints, expressed as tolerances on the closed-loop transfer functions. For this project, the synthesis was based on the set of specifications defined by the SISO-QFTIT computational tool provided by Sysquake Runtime.

3.5.1 System Model for Controller Design

To capture the system dynamics under real operating conditions, the system was characterized using four different load scenarios: unloaded operation (without a patient) and experimental tests with three volunteer subjects. The inclusion of multiple subjects enables a more robust and detailed definition of the parametric uncertainty space, improving the model's representativeness of biomechanical variability compared to preliminary characterizations.

From the experimental identification data, an average model, denoted as $G_{avg}(s)$, was initially obtained. However, using strict averaging carries the risk of designing the controller based on a "virtual" model that lacks physical representativeness, potentially distorting frequency-domain analysis. For this reason, a transfer function that best represented the central and physically realizable behavior of the system was selected from the experimental data. This empirical response was designated as the *nominal plant* $G_{nom}(s)$. The relationship between the average model and the nominal model adopted for the design is expressed as:

$$G_{avg}(s) = \frac{0.02695}{s(s+2.165)} \quad \longrightarrow \quad G_{nom}(s) = \frac{0.02937}{s(s+2.718)} \tag{3.30}$$

In order to account for the range of dynamics generated by users' biomechanical differences (variations in arm mass and inertia) and the inherent mechanical friction of the exoskeleton, a parametric uncertainty of ±20% was introduced on the gain and pole of the nominal system. This defines the family of uncertain plant models $\mathcal{G}$, which constitutes the fundamental basis for computing the templates in QFT synthesis:

$$\mathcal{G} = \left\{ G(s) = \frac{k}{s(s+a)} : k \in [0.0235, 0.03524],\ a \in [2.174, 3.262] \right\} \tag{3.31}$$

Finally, it is necessary to limit the control action in accordance with the physical constraints of the hardware. The exoskeleton actuator operates within a safe voltage range of ±12 V. An overly aggressive QFT design would generate signals that quickly exceed this threshold. Such actuator saturation not only invalidates the theoretical guarantees of stability and performance, but also poses a risk of damage to the motor and associated electronics. Consequently, loop shaping was performed under a practical trade-off criterion: ensuring robustness without requiring a control effort that exceeds the physical limitations of the actuator.

3.5.2 Constructing uncertainty templates

For the construction of the uncertainty templates from the plant family $\mathcal{G}$, the definition of the operating frequency vector Ω was derived strictly from the biomechanical parameters of the rehabilitation therapy. Since direct physical interaction between the exoskeleton and the patient makes high-frequency dynamic requirements practically irrelevant, the evaluation points were determined based on the time required to complete a joint movement cycle (flexion and extension) at different actuator voltage levels. These values, detailed in Table 2, define the system's operating spectrum, focusing exclusively on the initial stages of passive therapy.

Table 2

Clinical and control parameters according to the voltage applied to the actuator.

V [V]	t Mov. [s]	Vel. [°/s]	ω [rad/s]	Phase
2	27.00	0.98	0.1164	Hyperacute
4	22.50	1.18	0.1396	Hyperacute
6	18.00	1.48	0.1745	Hyperacute
8	13.50	1.97	0.2327	Hyperacute
10	9.00	2.95	0.3491	Hyperacute
12	4.50	5.91	0.6981	Acute

To evaluate disturbance rejection under spasticity episodes, an upper critical frequency was included in the Ω vector. Assuming a sudden spasm of $60^\circ/\mathrm{s}$, an equivalent frequency of $\omega_p = \frac{2\pi}{6} \approx 1.047$ rad/s is obtained. Its inclusion ensures that the control action mitigates these movements without destabilizing the system.

Furthermore, since the QFT design is carried out in the pseudo-continuous w-domain for subsequent digital implementation ($T_s = 0.03$ s), it is necessary to apply frequency mapping (*pre-warping*). The nonlinear relationship between the original physical frequency (ω) and the transformed frequency (ν) is given by:

$$\nu = \frac{2}{T_s} \tan\left(\frac{\omega T_s}{2}\right) \tag{3.32}$$

Although the clinical operating frequencies described above are low and therefore the frequency warping effect is minimal performing the synthesis directly in the w-domain while accounting for this mapping constitutes a measure of mathematical rigor. This ensures the absence of approximation errors when evaluating compliance with the specifications during the discretization stage. Applying this transformation to the original vector of clinical frequencies and the critical spasm frequency yields the set of mapped frequencies (w_ν) used internally by the software for template generation:

$$w_v = \{0.1164, 0.1396, 0.1745, 0.2327, 0.3491, 0.6982, 1.0472\}\ \text{rad/s}$$

Once the plant family has been evaluated over the equivalent frequency vector, the results are projected onto the Nichols diagram, as illustrated in Figure 13. Each closed contour (polygon) defines the uncertainty template for a given frequency w_{v_i}, while the circular marker within it indicates the geometric location of the nominal plant G_{nom}. The area of these templates provides a direct visual indication of the level of parametric uncertainty; greater dispersion (larger templates) imposes a more stringent geometric constraint on the loop-shaping algorithm when satisfying the design specifications without violating exclusion regions.

Figure 13

Nichols diagram with uncertainty templates and nominal plant

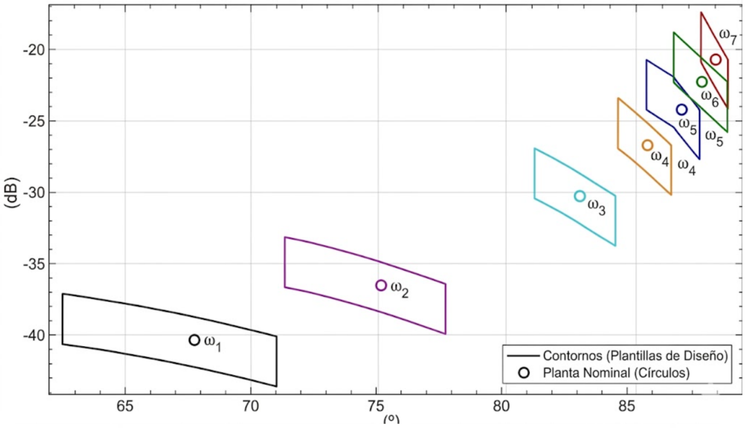

3.5.3 *Performance Specifications and Constraints in the Nichols Plane*

To carry out the synthesis of the robust controller, it is essential to formally establish the maximum allowable tolerances. These tolerances are defined through weighting functions (W_s) that bound stability, disturbance rejection, and trajectory tracking behavior. Table 3 summarizes the four critical specifications required for safe exoskeleton operation, detailing their analytical expressions and the limit values (K_w) configured in the design environment.

From these exact definitions, the QFT methodology translates each inequality into geometric

Table 3

Design specifications for the QFT-based robust control of the exoskeleton.

Type	Description	Mathematical Expression	Value (K_w)
1	Robust Stability	$\left\lvert\frac{PC}{1+PC}\right\rvert \leq W_{s1}$	1.2000
2	Disturbance Rejection (Output)	$\left\lvert\frac{1}{1+PC}\right\rvert \leq W_{s2}$	1.0608
3	Disturbance Rejection (Input)	$\left\lvert\frac{P}{1+PC}\right\rvert \leq W_{s3}$	0.1000
6	Reference Tracking	$W_{s6a} \leq \left\lvert\frac{PC}{1+PC}\right\rvert \leq W_{s6b}$	[0.5393 , 3.41e-2]

constraints (*bounds*) in the Nichols diagram. These bounds define exclusion regions that the nominal open-loop function $L_0(s)$ must not encroach upon, ensuring that the entire family of uncertain plants $\mathcal{G}$ satisfies the design requirements. To preserve the readability of the document, the detailed Nichols diagrams corresponding to each computed bound have been compiled in **Appendix G**.

Robust Stability (Type 1): This constraint limits the resonance peak of the complementary sensitivity function. By defining $W_{s1} = 1.2$, the minimum phase (M_f) and gain (M_g) margins are established as:

$$M_f \geq 2\arcsin\left(\frac{1}{2(1.2)}\right) = 2\arcsin(0.4167) \approx 49.2^\circ \tag{3.33}$$

$$M_g \geq \frac{W_{s1}}{W_{s1} - 1} \qquad \Longrightarrow \qquad M_{g(\mathrm{dB})} = 20\log_{10}(6) \approx 15.56 \text{ dB} \tag{3.34}$$

These values ensure compliance with commonly recommended margins (phase margin between 45° and 50°, and gain margin between 1.5 and 2.0). This specification was primarily evaluated at the lowest frequencies of interest (ω_1 **and** ω_2). Inspection of the corresponding bounds in the Nichols diagram shows wide regions, indicating that within this bandwidth the system does not exhibit critical instability tendencies under parametric uncertainty.

Output Disturbance Rejection (Type 2): Once stability is guaranteed, the analysis focuses on robustness against involuntary patient movements. Although the mechanical structure of the exoskeleton inherently resists abrupt variations, the controller is designed to actively reject such disturbances. The corresponding bounds were computed over the frequency range between ω_2 and ω_6.

Input Disturbance Rejection (Type 3): For input disturbances (voltage), measurements obtained from the ADRC observer were considered. It was established that a muscle spasm equivalent to a 1 V disturbance at the actuator should not produce an angular deviation greater than 0.1 rad (maximum tolerance of 10%). Given the clinical relevance of this requirement for patient safety, the bounds were computed over the entire design frequency range, from ω_1 to ω_7.

Robust Reference Tracking (Type 6): Finally, trajectory tracking requires that the dynamic response of the entire plant family be contained within a prescribed performance envelope (*tube*). To achieve this, two bounds were defined:

- **Upper Bound (W_{s6a}):** Modeled with a 5% overshoot and a settling time of 8 s.
- **Lower Bound (W_{s6b}):** Modeled with 0% overshoot and a settling time of 20 s.

Since the reference input of the exoskeleton is of ramp type, it is essential to mitigate overshoot in order to avoid abrupt movements. Furthermore, the static gain of these functions was constrained to 0 dB to preserve the reference magnitude in radians. It is important to note that this specification bounds the maximum allowable spread of the responses, but does not inherently guarantee that they lie within the envelope. To enforce strict tracking, the final stage consists of designing a pre-filter $F(s)$ specifically for this purpose.

3.5.4 Controller Synthesis (Loop-shaping) and Pre-filter

The loop-shaping stage is carried out in the Nichols diagram. In this domain, the software overlays all performance bounds computed in the previous section, retaining the most restrictive constraint at each frequency. The intersection of these constraints generates a global boundary (*composite bound*) that defines exclusion regions which the nominal open-loop trajectory must strictly avoid:

$$L_0(j\omega) = P_0(j\omega)C(j\omega) \tag{3.35}$$

Figure 14

Nominal open-loop trajectory on the Nichols diagram.

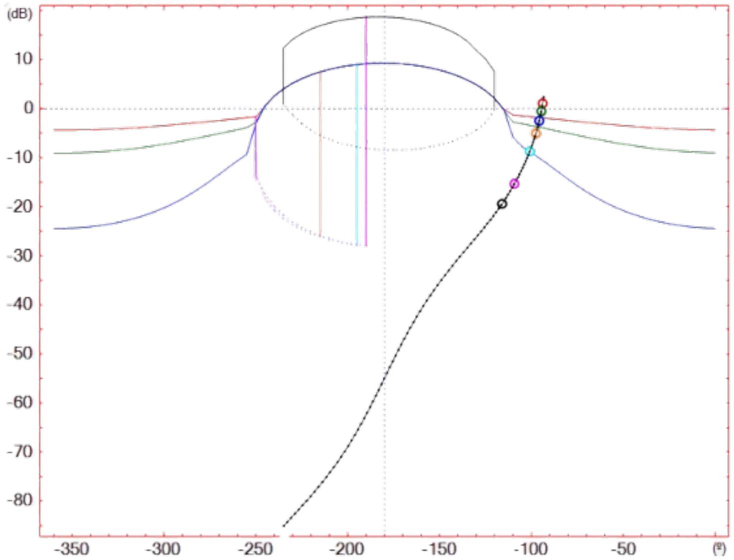

The main objective in this phase is to introduce singularities (poles and zeros) and adjust the controller gain $C(s)$ such that the L_0 curve satisfies all exclusion regions with minimal mathematical complexity. Initially, the feasibility of meeting the specifications using only proportional control (gain adjustment) was evaluated. Although this approach positioned the curve outside the robustness bounds, the resulting system exhibited excessive dynamic spread, making it impossible to design a suitable pre-filter to achieve reference tracking across the plant family.

Consequently, additional geometric flexibility was introduced by incorporating a controller structure with one pole and one zero. A critical aspect during this synthesis was phase adjustment. To ensure compliance with the Nyquist stability criterion, a negative static gain was applied to the controller. This choice induces a $-180°$ shift in the nominal trajectory, relocating it to the stable region on the right-hand side of the Nichols diagram, as illustrated in Figure 14. It should be noted that the effect of this negative sign is later compensated in the physical implementation.

$$C(w) = -10.5692\left(\frac{w+0.8}{w+0.7}\right) \tag{3.36}$$

Additionally, the strategic placement of the pole and zero at low frequencies proved essential in limiting the control effort. By concentrating the compensator dynamics in this region, amplification of high-frequency components is avoided, and a controlled roll-off is introduced just beyond the useful bandwidth. This prevents aggressive control actions and ensures that the control signal remains within the actuator's physical limits (±12 V).

With stability and disturbance rejection ensured by $C(w)$, the synthesis of the pre-filter $F(w)$ guarantees that the tracking response of the entire plant family $\mathcal{G}$ remains within the specified bounds (Type 6). The design consists of adjusting the static gain to shift the responses into the admissible region and incorporating a pole-zero network to shape the frequency response, eliminating transient overshoot according to the following structure:

$$F(w) = 0.648\left(\frac{w+3.7}{w+2.2}\right) \tag{3.37}$$

The effectiveness of this conditioning is visually verified in Figure 15. As can be seen in the magnitude diagram, when $F(w)$ is applied, the dispersion of the plant family is strictly contained between the upper (red) and lower (blue) bounds. This confirms robust tracking, ensuring that the exoskeleton responds to rehabilitation trajectories with the calculated biomechanical precision and smoothness.

Figure 15

Magnitude response of the system with pre-filter.

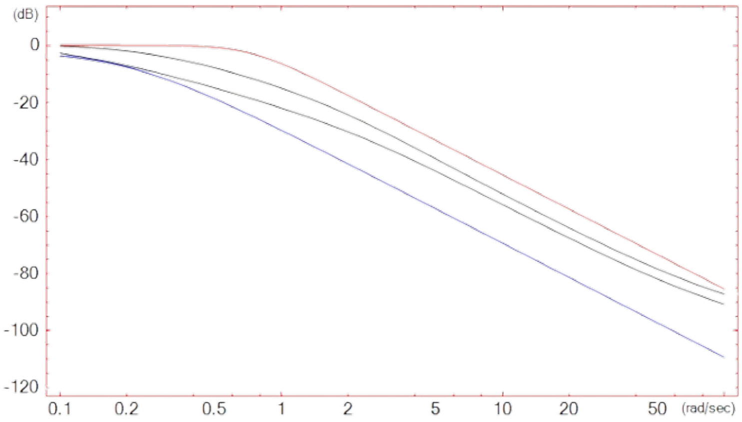

3.5.5 Discretization of the controller and the pre-filter

As justified in the definition of the frequency vector, the entire QFT synthesis (shaping of C and F) was carried out in the pseudo-continuous domain w. This methodological decision is not trivial. Attempting to design a controller in the continuous domain s and then discretizing it directly into the z domain using numerical methods usually generates severe distortions in the frequency response, especially when approaching the Nyquist frequency. In contrast, the adopted design scheme guarantees the preservation of the robustness specifications. The complete flow of transformations followed in this work is summarized in the following analytical sequence:

$$P(s) \xrightarrow{\text{ZOH}} P(z) \xrightarrow{\text{Tustin}} P(w) \xrightarrow{\text{QFT}} C(w) \xrightarrow{\text{Tustin}^{-1}} C(z)$$

Following the final step of this sequence, the transfer functions of the controller $C(w)$ and the pre-filter $F(w)$, obtained after loop-shaping, are transformed to the digital domain z. For this procedure, the inverse bilinear transformation (inverse Tustin) is applied, using the same sampling period $T_s = 0.03$ s with which the original pre-warping was performed. The result of this operation yields the final discrete algorithms in the form of difference equations, ready to be coded in the exoskeleton microcontroller. Applying this transformation, the final expressions for control and filtering are obtained:

$$C(z) = \frac{10.62z - 10.37}{z - 0.9866} \quad ; \quad F(z) = \frac{0.662z - 0.5919}{z - 0.935} \tag{3.38}$$

3.5.6 Simulation of the controller

To validate the performance of the controller $C(z)$ and the pre-filter $F(z)$, discrete numerical simulations were carried out in the MATLAB environment. In order to establish a standardized evaluation framework and allow direct comparison, the same testing methodology and reference signals previously used in the validation of the ADRC controller in this project were adopted.

The implemented reference signal $\theta_{ref}(t)$ corresponds to a periodic trapezoidal profile, which faithfully emulates the repetitive flexion and extension trajectories used in hand rehabilitation therapies. As in the ADRC analysis, the linear magnitudes of the therapy were scaled using the geometric factor of the mechanism ($r_1 = 43$ mm) to transform displacement into a direct angular position reference.

Figure 16

Reference tracking and system control signal.

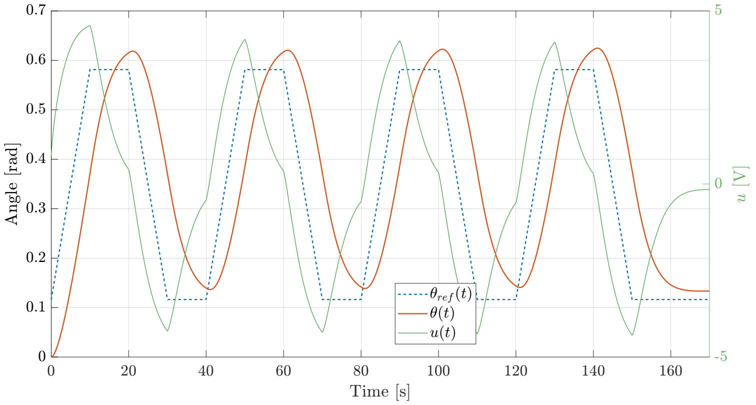

It is important to note a slight time delay between the reference and the actual output; this delay is a consistent and deliberate consequence of the settling time of 8 s configured in the loop-shaping stage, prioritizing smoothness of movement at all times. Additionally, the control signal $u(t)$ (illustrated on the secondary axis) operates smoothly and without aggressive variations, remaining well within the physical saturation limits of the actuators (±12 V). This confirms that the preventive design of high-frequency gain roll-off was successful.

To evaluate the robustness of the closed-loop system, a stress test was performed by injecting an external disturbance $\psi(t)$ directly at the plant input. Unlike the ADRC approach, where unmodeled dynamics are actively estimated by an observer, in this QFT validation stage the disturbance is purely simulated.

Figure 17

Reference tracking and system control signal.

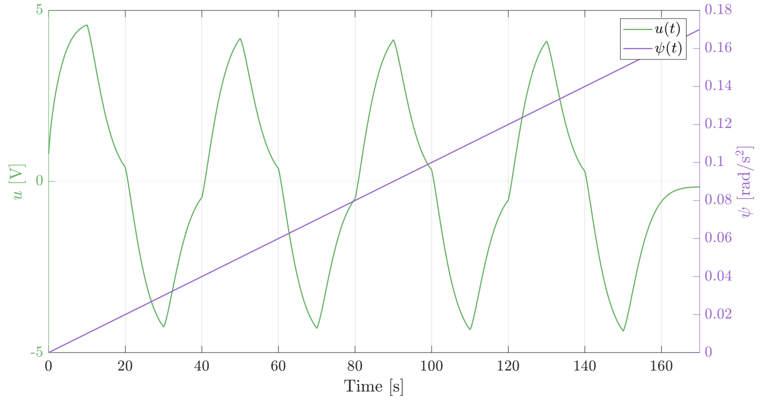

Initially, a ramp-type disturbance with constant slope was introduced, which allows emulating a progressive resistance force exerted by the user, a typical behavior in patients who develop increasing spasticity during therapy. When analyzing the system response, it is observed that, to compensate for this progressive input, the control action $u(t)$ reacts in an inversely proportional manner; that is, the control effort begins to decrease (lose strength) gradually and steadily. This progressive reduction in voltage is the mechanism by which the controller actively cancels the error and mitigates the force of the spasm.

As shown in Figure 17, the controller's rejection capability against the ramp is highly effective. However, it is essential to emphasize that this performance is conditioned by the physical limits of the actuators. Since the design considered a strict voltage constraint, if the disturbance were to continue growing indefinitely, the control signal would reach its saturation limit at -12 V. At that point, the system would lose its active disturbance rejection capability, resulting in a deterioration of reference tracking. This is a limitation inherent to the hardware power constraints and not to the theoretical architecture of QFT.

3.5.7 Hardware Implementation of the QFT Controller

As detailed in the implementation of the ADRC controller, the experimental validation was carried out on a shared architecture based on an ESP32 microcontroller with a sampling period of $T_s = 0.03$ s. In this environment, the VL6180X sensor is used assuming ideal dynamics $H(s) = 1$, justified by the linearity and speed of optical time-of-flight technology. However, any physical measurement introduces high-frequency noise that must be managed. This is where both strategies differ substantially: while the state-space scheme requires adding complex digital filters to prevent noise from destabilizing its observer, the QFT design takes advantage of its native gain roll-off to mitigate it inherently. This allows obtaining a clean feedback signal using only the basic statistical filters already integrated into the shared code.

The main advantage of this strategy lies in computational efficiency. While ADRC requires processing heavy matrices in real time, the QFT controller is executed through difference equations that only involve simple scalar operations. In each interrupt cycle, the ESP32 computes the control action $u[k]$ based on the current and past values of the error $e[k]$ and the previous voltage, following an easily computable recursive structure:

$$u[k] = b_0 e[k] + b_1 e[k-1] + \cdots - a_1 u[k-1] - \dots \tag{3.39}$$

This format optimizes processing resources by avoiding the use of linear algebra libraries, allowing the microcontroller to execute the control law quickly and deterministically, ensuring the temporal stability of the system.

Finally, the computed numerical effort is translated into a PWM signal to drive the motor system. As a clinical safety and hardware protection mechanism, a strict software constraint was implemented to limit the control action to the physical bounds of the electromechanical actuator

(±12 V). This empirical saturation acts as a final barrier against abnormal disturbances or muscle spasms, validating in the physical domain the control effort constraints that were mathematically imposed during the synthesis in the Nichols diagram.

3.5.8 QFT Control Technique Results

The designed and implemented QFT-based controller was experimentally evaluated in three different scenarios, in the same way as was done for the ADRC controller. Figure 18 presents the results corresponding to User 1, Figure 19 shows the results obtained for User 2, and finally, Figure 20 presents the results of the system without a user.

Figure 18

Results of the QFT-based controller for User 1.

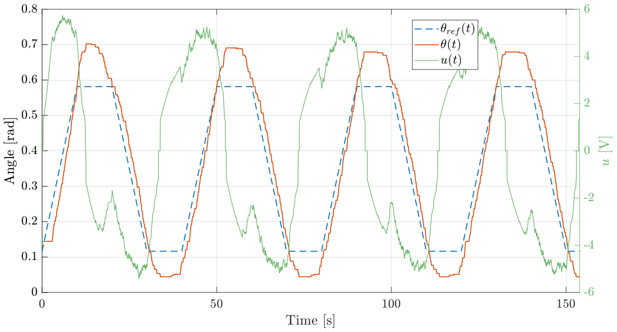

Figure 19

Results of the QFT-based controller for User 2.

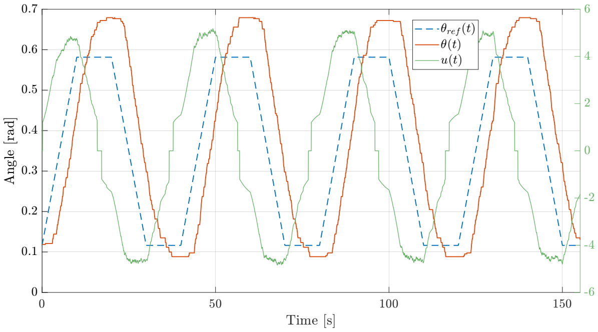

Figure 20

Results of the QFT-based controller without a user.

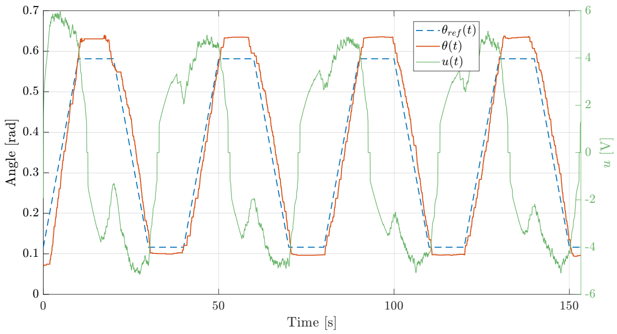

When analyzing the experimental responses, the loaded scenarios (Figures 18 and 19) exhibit smooth, continuous tracking without overshoot. The slight time delay is due to design constraints oriented toward biomechanical safety, keeping the control effort within safe margins (≈ 5 V). In contrast, in the no-user test (Figure 20), the drastic reduction in mechanical impedance shifts the plant dynamics outside the calculated uncertainty templates, generating an overshoot of 0.68 rad. Despite this deviation in tracking, the system does not exhibit unstable oscillations or voltage saturation, which practically validates the robust stability of the QFT design under extreme dynamic variations.

3.6 Comparative Analysis

To establish a reference point for evaluating the performance of the designed controllers, a proportional controller was implemented under the same experimental conditions previously considered for the ADRC and QFT controllers.

The proportional controller was defined based on the ADRC control law structure, considering only the constant k_0 associated with position state feedback. In this sense, by using exclusively the state $x_0 = \theta$ in the feedback, the resulting control action is equivalent to that of a classical proportional controller, where the control signal depends solely on the position error. The equivalent proportional constant k_p was assigned a numerical value of 34.

Figure 21 presents the results corresponding to User 1, Figure 22 shows the results obtained for User 2, and finally, Figure 23 presents the behavior of the system without a user.

Figure 21

Results of the proportional controller for User 1.

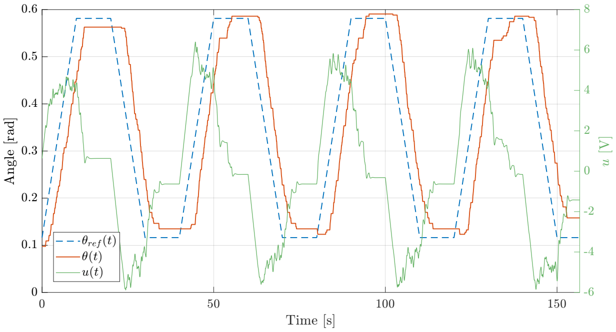

Figure 22

Results of the proportional controller for User 2.

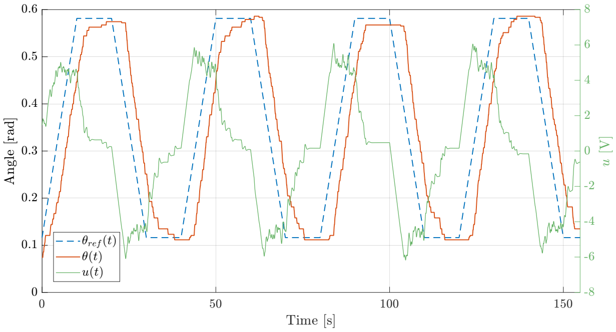

Figure 23

Results of the proportional controller without a user.

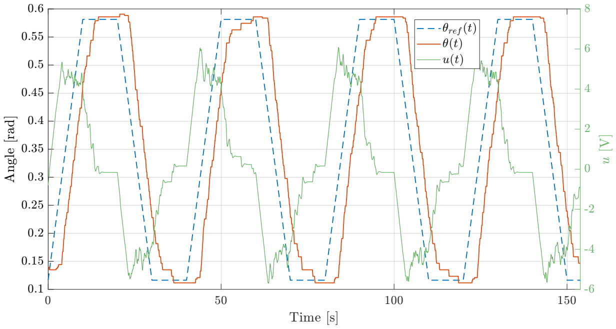

The comparison between the different strategies was carried out using a set of time-domain performance indices, specifically the integral of the absolute value of the control (IAU), the integral of the absolute error (IAE), the integral of the squared error (ISE), the integral of the time-weighted absolute error (ITAE), and the integral of the time-weighted squared error (ITSE). These criteria were selected because they allow a complementary characterization of both the control effort required by each strategy and the quality of reference tracking, including the magnitude of the error, its persistence over time, and the penalization of late deviations.

Under this approach, the comparison is performed in a homogeneous manner between controllers, evaluating their performance under variations in the mechanical interaction of the system, such as changes in load and in the dynamic characteristics of the users. This allows a comprehensive analysis of the advantages and limitations of each strategy, not only in terms of tracking accuracy, but also considering the physical constraints of the system, such as actuator saturation and the need to maintain smooth and safe control actions for the user.

The performance indices calculated for each control strategy and operating condition are summarized in Table 4.

Table 4

Performance metrics for the controllers evaluated under different scenarios.

Scenario	Controller	IAU	IAE	ISE	ITAE	ITSE
User 1	QFT	539.2027	9.0785	0.6436	688.1829	47.3532
	ADRC	420.9478	9.7652	1.0306	745.2673	77.8312
	Proporcional	413.8525	12.1678	1.4323	963.1939	114.5625
User 2	QFT	487.2444	18.3883	2.9594	1442.8000	234.9311
	ADRC	440.7377	10.1028	1.0908	773.9459	84.1555
	Proporcional	409.3404	12.0356	1.4424	927.7240	112.1053
No user	QFT	524.1820	6.0997	0.3086	450.3756	20.8900
	ADRC	417.9332	9.8211	1.0361	748.5627	79.0327
	Proporcional	391.6437	11.5155	1.3676	888.4715	105.8284

From the obtained results, a clear trade-off between control effort and tracking quality is evident for the different evaluated strategies. The proportional controller consistently presents the lowest values of the IAU index, indicating a lower demand on the actuator; however, this behavior is accompanied by a significant increase in the error indices (IAE, ISE, ITAE, and ITSE), reflecting lower accuracy and greater persistence of the error over time.

In contrast, the QFT-based controller generally exhibits a higher control effort, especially under conditions with user interaction, which suggests a more aggressive control action. Although in some scenarios it manages to reduce certain error indices, its performance shows considerable variability between operating conditions, evidencing greater sensitivity to changes in load and system dynamics.

For its part, the ADRC controller presents the most consistent behavior among all the analyzed cases. Unlike the other strategies, it maintains similar values in the error indices for the three evaluated scenarios, particularly in those weighted in time (ITAE and ITSE), which indicates that the tracking quality does not strongly depend on the operating condition. This low variability in performance suggests a greater capacity to adapt to disturbances and changes in mechanical interaction, achieving more uniform tracking of the reference.

Overall, these results show that, although proportional control is efficient from an energy standpoint, it sacrifices performance, while QFT can improve the response in certain cases at the cost of greater control effort and lower consistency. In this context, ADRC stands out as the strategy that offers the best overall trade-off, combining a moderate control effort with robust and consistent performance under real operating conditions of the system.

4. Conclusions

The mathematical modeling of the system, together with the experimental identification process carried out, allowed obtaining an adequate representation of the exoskeleton dynamics under different operating conditions. Based on this model, the ADRC and QFT control strategies were fully designed and implemented, fulfilling the objectives of the project. During this stage, it was necessary to adjust the designs considering the physical limitations of the system, particularly actuator saturation, which was identified as the main constraint in the practical implementation of the controllers.

From the experimental validation, the main advantages and disadvantages of each strategy were identified through the analysis of performance indices associated with tracking error and control effort. The results show that the ADRC controller presents better overall behavior in the presence of unmodeled dynamics and unknown disturbances, maintaining consistent performance across the different evaluated scenarios. On the other hand, the QFT-based controller, by considering a reduced set of parametric uncertainties, showed limited robustness against broader variations in operating conditions, reflected in greater variability in its performance.

In general terms, the implemented controllers allow adequate reference tracking, generating motion profiles that meet the average velocity and characteristic time requirements associated with therapy conditions, which validates their applicability in the context of the developed system.

Finally, this work provides a comparative evaluation of two advanced control approaches applied to a robotic rehabilitation system, highlighting their strengths and limitations under real experimental conditions. These results contribute to the development of more robust and adaptive control strategies and provide relevant criteria for the selection of control techniques in human-machine interaction systems.

5. Recommendations

Based on the results obtained during the implementation and experimental validation of the system, several opportunities for improvement were identified in the physical design of the exoskeleton, both at the mechanical level and in the sensing systems.

Regarding the mechanical design, the need to implement improvements in the transmission mechanism responsible for finger movement is evident, since the current system presents limitations associated with efficiency and response speed, which directly impacts the overall performance of the exoskeleton. Likewise, it is recommended to redesign the way in which the different parts of the device are coupled, with the objective of facilitating its assembly, maintenance, and repair, which are fundamental aspects in clinical applications where system availability and reliability are critical.

On the other hand, the selected actuators were not the most suitable for the application. The use of low-power geared motors, together with a worm gear mechanism, introduces a high reduction ratio that significantly limits the system's movement speed. As a consequence, high voltage levels are required to achieve fast responses, which increases the probability of saturation in the control signal, especially when implementing strategies such as ADRC that include active disturbance cancellation. This phenomenon becomes particularly critical when low settling times are required, since the control action tends to reach the physical limits of the actuator.

In this regard, it is recommended to consider the use of actuators with higher power capacity or, alternatively, to redesign the transmission mechanism using configurations other than a worm gear, which allow for a faster and more efficient response. Additionally, it is important to highlight that the current mechanism exhibits self-locking behavior, which prevents passive movement of the fingers when the motors are not operating. This characteristic makes it difficult to place the device on the user, so it is suggested to evaluate mechanisms that facilitate interaction with the patient.

Regarding the sensing system, the distance sensor used presents significant noise levels when configured to operate at high sampling frequencies. This condition directly affects the performance of the control algorithms, particularly in schemes such as ADRC, where the noise is interpreted as part of the total disturbance. For this reason, it is recommended to explore sensing alternatives that offer a higher signal-to-noise ratio and a better dynamic response. Likewise, it would be advisable to consider integrating the sensing system with the proposed mechanical redesign, in such a way that a more robust measurement consistent with the real dynamics of the exoskeleton is achieved.

Additionally, beyond the type of sensor used, it is advisable to consider the implementation of an independent sensing system for each finger. In the current configuration, where a single sensor represents the global movement of the mechanism, increasing phase differences may arise between the fingers as they move, due to differences in their geometric paths and variations in the individual frictions of each joint. This effect introduces errors in the representation of the real state of the system, affecting control accuracy. In this sense, incorporating individual sensors would allow for a more faithful measurement of each finger's movement, enabling more precise and decoupled control strategies. However, this improvement would also imply modifications in the electronic design of the system, particularly in the PCB, in order to allow independent actuation of each actuator, since in the current implementation all motors share the same control signal.

Bibliography

Barry, A. J., Kamper, D. G., Stoykov, M. E., Triandafilou, K., & Roth, E. (2022). Characteristics of the severely impaired hand in survivors of stroke with chronic impairments [Cited by: 18]. *Topics in Stroke Rehabilitation*, *29*(3), 181–191. https://doi.org/10.1080/10749357.2021.1894660

Carreño Jerez, C. F., Pinto Orozco, J. E., & Candamil Téllez, J. G. (2026). *Monitoreo y control de un exoesqueleto para terapia robótica bilateral en pacientes post-acv* [Director: Rodolfo Villamizar Mejía. Co-directores: Jorge Eduardo Quintero, María Solange Patiño].

Carreño Zagarra, J. J. (2020). *Robust control approach for multivariable systems under delays, parametric uncertainty and external disturbances* [Tesis de Maestría]. Universidad Industrial de Santander [Magíster en Ingeniería Electrónica, Facultad de Ingenierías Fisicomecánicas, Escuela de Ingenierías Eléctrica, Electrónica y de Telecomunicaciones].

Garcia-Sanz, M. (2017a). *Robust control engineering: Practical qft solutions*. CRC Press. https://doi.org/10.1201/9781315215091

Garcia-Sanz, M. (2017b). *Robust control engineering: Practical qft solutions*. CRC Press. https://doi.org/10.1201/9781315215091

Gu, S., Ye, Z., Zhang, L., Peng, R., Wang, J., & Li, H. Research on a novel hand exoskeleton rehabilitation training system [Cited by: 2]. In: Cited by: 2. 2024, 496–501. https://doi.org/10.1109/ICMA61710.2024.10632949

Gu, S., Ye, Z., Zhang, L., Peng, R., Wang, J., & Li, H. Research on a novel hand exoskeleton rehabilitation training system [Cited by: 2]. In: Cited by: 2. 2024, 496–501. https://doi.org/10.1109/ICMA61710.2024.10632949

Horowitz, I. (1991). Survey of quantitative feedback theory (qft). *International Journal of Control*, *53*(2), 255–291. https://doi.org/10.1080/00207179108953619

Houpis, C. H., Rasmussen, S. J., & Garcia-Sanz, M. (2006). *Quantitative feedback theory: Fundamentals and applications* (2nd). CRC Press. https://doi.org/10.1201/9781420019080

Jones, C. L., Wang, F., Osswald, C., Kang, X., Sarkar, N., & Kamper, D. G. (2010). Control and kinematic performance analysis of an actuated finger exoskeleton for hand rehabilitation following stroke. *2010 3rd IEEE RAS and EMBS International Conference on Biomedical Robotics and Biomechatronics*, 282–287. https://doi.org/10.1109/BIOROB.2010.5626057

Mathonsi, T., Abozaid, H. M., Sikhakhane, K., Berman, T., Rimer, S., Salifu, M., Tivani, L., & Rawat, M. An overview of a robotic hand rehabilitation system [Cited by: 3]. In: Cited by: 3. 2024. https://doi.org/10.1109/ICECER62944.2024.10920306

Mathonsi, T., Abozaid, H. M., Sikhakhane, K., Berman, T., Rimer, S., Salifu, M., Tivani, L., & Rawat, M. An overview of a robotic hand rehabilitation system [Cited by: 3]. In: Cited by: 3. 2024. https://doi.org/10.1109/ICECER62944.2024.10920306

Norman, S. S., Jamaludin, J., & Ab Malik, N. (2024). Advancements in hand assistive technologies for stroke rehabilitation: A systematic review of mechanisms and innovations. *IEEE Access*.

Rosewilliam, S., Pandyan, A. D., & Roskell, C. A. (2014). *Goal setting in stroke rehabilitation: Theory, practice and future directions* [Cited by: 3]. https://doi.org/10.1201/b17166

Singh, N., Saini, M., Kumar, N., Srivastava, M. V. P., & Mehndiratta, A. (2021). Evidence of neuroplasticity with robotic hand exoskeleton for post-stroke rehabilitation: A randomized controlled trial. *Journal of NeuroEngineering and Rehabilitation*, *18*(1), 76. https://doi.org/10.1186/s12984-021-00867-7

Spong, M. W., Hutchinson, S., & Vidyasagar, M. (2020). *Robot modeling and control* (2nd). John Wiley & Sons.

Tran, P., Jeong, S., Herrin, K. R., & Desai, J. P. (2021). Review: Hand exoskeleton systems, clinical rehabilitation practices, and future prospects. *IEEE Transactions on Neural Systems and Rehabilitation Engineering*, *29*, 2261–2276. https://doi.org/10.1109/TNSRE.2021.3122144

Worsnopp, T., Peshkin, M., Colgate, J., & Kamper, D. (2007). An actuated finger exoskeleton for hand rehabilitation following stroke. *2007 IEEE 10th International Conference on Rehabilitation Robotics*, 896–901. https://doi.org/10.1109/ICORR.2007.4428530